

NASA Technical Paper 1579

# Investigation of Flow Characteristics Over Missile Bodies at Supersonic Speeds

Raymond L. Barger and Wallace C. Sawyer

DECEMBER 1979

**CASE FILE  
COPY**

**NASA**

NASA Technical Paper 1579

# Investigation of Flow Characteristics Over Missile Bodies at Supersonic Speeds

Raymond L. Barger and Wallace C. Sawyer  
*Langley Research Center*  
*Hampton, Virginia*



National Aeronautics  
and Space Administration

**Scientific and Technical  
Information Branch**

1979

## SUMMARY

Three missile body shapes were tested at Mach numbers of 1.50, 2.16, and 2.86 with angles of attack up to  $30^\circ$ . At moderate angles of attack, the flow was not characterized by a uniform pattern or by periodic vortex shedding. Flow visualization indicated cumulative effects due to shed vorticity. The pitching-moment variation was a sensitive indicator of incipient separation. Vortex effects were observed more readily with oil-flow visualization than with vapor-screen or schlieren methods. The cross-flow drag appeared to be primarily a function of cross-flow fineness ratio.

## INTRODUCTION

The body of literature dealing with the flow over missile body configurations has grown rapidly, largely as a result of concern over asymmetric separation phenomena (ref. 1). The flow pattern at high angles of attack has been studied analytically by the impulsively started cylinder analogy, a kind of two-dimensional cross-flow method (ref. 1).

For slender bodies at low angles of attack (less than about  $5^\circ$ ) where separation is negligible, the linear model of the flow as a superposition of a two-dimensional cross-flow on the axial flow is valid. According to slender-body theory, the forces determining the lift and pitching moment under these conditions are associated with varying cross sections over the nose section of the missile body. However, the forces over the constant-geometry section of the body become significant and eventually predominate when the angle of attack reaches a value for which separation occurs. The rapid increase in normal force is due to the increase in cross-flow drag. At moderate angles of attack ( $5^\circ$  to  $30^\circ$ ), missiles which do not have a large ratio of afterbody-to-nose length do not develop uniform flow over a significant part of the afterbody. Aft of the shoulder, the flow pattern undergoes a relatively long transitional phase. A study of this transitional flow pattern is the primary subject of this report. Three missile bodies with different cross-sectional shapes were used in an experimental investigation to study the interaction of the cross flow with the axial flow and the possible delay of separation to a higher angle of attack. Bodies with various cross-section shapes have been tested previously (ref. 2), but the shapes for the present study were specifically designed for the purpose of obtaining some insight into the nature of the flow.

## SYMBOLS

The aerodynamic coefficients are referred to the body-axis system. The moment reference was located aft of the nose tip at 43.44 percent of body length. Dimensions are given in SI units with U.S. Customary Units in parentheses.

A maximum cross-sectional body area of models A, B, and C, 20.3 cm<sup>2</sup>

$C_A$  axial-force coefficient,  $\frac{\text{Axial force}}{qA}$

$C_l$  rolling-moment coefficient,  $\frac{\text{Rolling moment}}{qAd}$

$C_m$  pitching-moment coefficient,  $\frac{\text{Pitching moment}}{qAl}$

$C_N$  normal-force coefficient,  $\frac{\text{Normal force}}{qA}$

$C_n$  yawing-moment coefficient,  $\frac{\text{Yawing moment}}{qAd}$

$C_p$  pressure coefficient based on free-stream Mach number

$C_p^*$  pressure coefficient based on cross-flow Mach number

$C_Y$  side-force coefficient,  $\frac{\text{Side force}}{qA}$

d reference body diameter, 5.1 cm

h maximum body height, cm

l reference body length, 38.1 cm

M Mach number

q dynamic pressure, Pa

r radius measured from model centerline, cm



x	distance from nose apex measured along model centerline, cm
y	vertical distance, cm
$\alpha$	angle of attack, deg
$\beta$	angle of sideslip, deg
$\theta$	angular position measured counterclockwise about centerline of model (fig. 1), deg

## APPARATUS AND TESTS

### Tunnel

The investigation was conducted in the low Mach number test section of the Langley Unitary Plan wind tunnel. The test section has a cross-sectional area of 1.22 m<sup>2</sup> and a length of 2.13 m. The tunnel nozzle is of the asymmetric sliding-block type, which permits a continuous variation in Mach number from about 1.5 to 2.9.

### Models

Details of the three models are shown in figure 1 and photographs are shown in figure 2. Each model was 38.1 cm (15.0 in.) long with an afterbody cross-sectional area of 20.3 cm<sup>2</sup> ( $\pi$  in<sup>2</sup>). Model A was a body of revolution with an ogive nose section like that of the Sparrow missile (ref. 3). Models B and C had the same area distribution as model A, but with different cross-section shapes. They both had a maximum width about 0.93 times that of model A and a cross-section fineness ratio of 1.25. The lower half of the cross section of model B was a semicircle, but the upper half was designed to have a gradually varying curvature distribution in order to ease the adverse cross-flow pressure gradient. This theoretical cross-flow pressure distribution is compared with those of the other models in figure 3. For model C, the cross section consisted of a primary circular-arc fuselage section surmounted with a small circular-arc "canopy" section. This type of design tends to display attachment and secondary separation effects on the canopy part. Cross-flow pressure distribution (fig. 3), calculated by potential-flow theory, has limited applicability because, at moderate angles of attack, the cusp region near the juncture of the circular-arc sections tends to become filled with the vorticity resulting from separation.

### Tests

The force tests were conducted at Mach numbers 1.50, 2.16, and 2.86 with a constant Reynolds number of  $8.2 \times 10^6/\text{m}$  ( $2.5 \times 10^6/\text{ft}$ ). The angle-of-attack range was 0° to 30°.

An initial set of force and schlieren tests were run without transition grit on the models. Then a 1.60-mm (0.063 in.) strip of No. 50 grit was added circumferentially at the 3.05-cm (1.20 in.) station and No. 100 grit was distributed along the  $45^\circ$  and  $315^\circ$  meridian lines. All subsequent tests employed the gritted configurations.

For flow visualization purposes, the models were sprayed with black paint. White spots marked the  $90^\circ$  meridian at the 12.7-cm (5.0 in.) and 33.0-cm (13.0 in.) stations, and each meridian from  $90^\circ$  to  $180^\circ$  in  $22.5^\circ$  increments at the 22.9-cm (9.0 in.) station. Vapor-screen photographs were taken at Mach numbers of 2.16 and 2.86 with angles of attack of  $10^\circ$ ,  $15^\circ$ ,  $20^\circ$ , and  $30^\circ$ . Oil-flow photographs were taken at  $\alpha = 15^\circ$ ,  $20^\circ$ , and  $30^\circ$  for all bodies and Mach numbers and at  $\alpha = 25^\circ$  for some cases. Schlieren photographs were taken at  $\alpha = 10^\circ$ ,  $20^\circ$ , and  $30^\circ$  for all cases and at  $\alpha = 14^\circ$  or  $16^\circ$  for most cases.

### Measurements

Aerodynamic forces and moments were measured by means of a six-component strain-gauge balance which was housed within the body of the model. The balance was attached to a sting which, in turn, was rigidly fastened to the tunnel support system. Balance-chamber pressure was measured by means of a pressure orifice located in the balance chamber.

### Corrections

The angles of attack have been corrected for deflection of the balance and sting due to aerodynamic load and for tunnel up-flow angle. The drag and axial-force coefficients have been adjusted to correspond to free-stream static pressure acting over the base of the model.

## RESULTS AND DISCUSSION

### Force

The effect of transition on lateral forces is shown in figure 4. Some initial tests were run without fixed transition on the models. At the lowest Mach number tested ( $M = 1.50$ ), all of the models experienced some side force and yawing moment at  $\beta = 0^\circ$ , apparently as a result of asymmetric vortex shedding. Model B has a larger projected area in the lateral direction than model A and, consequently, larger lateral forces as shown in figure 4. Application of grit reduced these asymmetric forces (fig. 4) to virtually insignificant levels for all the models. This result indicates that, at these Mach numbers, the asymmetric vortex shedding at  $\beta = 0^\circ$  is primarily associated with the length of the laminar run.

Given in figure 5 are the normal-force, pitching-moment, and axial-force coefficients for all three models at the three test Mach numbers. At low angles of attack, the normal force is a linear function of  $\alpha$  as expected. In this range, the normal force is primarily lift which results from the increasing width of the model in the nose section, with negligible contribution from the afterbody. This is in accordance with slender-body theory (ref. 4). However, when the flow on the leeward side of the model begins to separate, another contribution to the normal force is added in the form of the cross-flow drag associated with the separated flow. Inasmuch as this separation occurs along the entire length of the afterbody, it acts on a sizable surface area and results in a rapid increase in normal force with increasing angle of attack.

The normal force for models B and C is smaller than for model A, both in the linear range at low angles of attack and in the nonlinear range. Since both B and C have a cross-section fineness ratio of 1.25, the normal forces on them should be nearly identical, but slightly lower than on model A. In the nonlinear range, the normal force, which is dominated by cross-flow drag, is virtually identical for models B and C. Since these two models have significantly different theoretical cross-flow pressure distributions but the same cross-section fineness ratio, it appears that cross-flow drag is more dependent on the cross-flow fineness ratio than on the design pressure distribution.

A method for estimating the contribution of the leeward-side separation to the normal force is given in reference 5. This semiempirical procedure is based primarily on experimental results obtained at subsonic speeds with asymmetric vortex shedding. The theory, however, is purported to be valid for any body of revolution with subsonic cross-flow Mach number.

A calculation of the cross-flow drag associated with separation was made by the method of reference 5 for model A at a free-stream Mach number of 1.50, for which the cross-flow Mach number is subsonic for all the test values of  $\alpha$ . Calculated and experimental values of the total normal force are compared in figure 6. Although the calculation indicates the correct trend of the data, it seriously underestimates the actual magnitude. This discrepancy is at least partly due to the fact that the separation effects in the present tests were essentially symmetric, whereas the theory was based primarily on an asymmetric vortex shedding model.

The pitching-moment data shown in figure 5 were obtained with the moment center 16.5 cm (6.5 in.) from the nose. This forward position of the moment center, only 5.1 cm (2.0 in.) aft of the shoulder, was chosen to increase the sensitivity of the data to the onset of cross-flow drag due to viscous effects, including separation.

The normal force can be described as the sum of a linear part associated with the nose region and a nonlinear part associated with the leeward separation. This description

is strongly supported by the pitching-moment results. At low angles of attack with fully attached flow, virtually no normal force was derived from the afterbody. The lift, which is associated with the nose region only, increases linearly with  $\alpha$  and gives a positive and increasing pitching moment. Once the flow begins to separate, however, the separation line extends to the base of the model, with stronger separation effects near the base than near the nose. Consequently, the pitching-moment curve experiences a rapid decrease in slope with the onset of separation, and the curve levels off and begins a sharp decline.

The lateral directional data shown in figure 7 for  $\beta = 3^\circ$  indicate that side forces and yawing moments for models B and C are larger than those for the body of revolution. At  $\alpha = 0^\circ$ , these forces are slightly higher for models B and C than for model A, as expected, because the laterally projected areas of the two asymmetric bodies are greater than that of model A. Thus, the pressures have a larger area on which to act. However, the large magnitude and variable nature of the lateral forces for positive values of  $\alpha$  indicate that they are associated with asymmetric vortex shedding.

#### Flow Visualization

The separation phenomenon is shown by oil-flow and vapor-screen techniques in figure 8 for model A at  $M = 2.16$  and  $\alpha = 15^\circ$ . The oil-flow photograph (fig. 8(a)) shows a separation line beginning in the vicinity of the shoulder at  $x = 11.4$  cm (4.5 in.) and  $\theta \approx 135^\circ$  and slanting downward to  $\theta \approx 100^\circ$  at  $x = 22.9$  cm (9.0 in.) and  $\theta \approx 85^\circ$  at  $x = 33.0$  cm (13.0 in.). A dark "well-scrubbed" region, resulting from strong vorticity in the flow field, begins to form at about the 22.9-cm (9.0 in.) station.

The corresponding vapor-screen photographs (fig. 8(b)) show no vorticity at  $x = 12.7$  cm (5.0 in.). At  $x = 22.9$  cm (9.0 in.), a symmetric pair of vortex sheets has formed near the body surface, and at  $x = 33.0$  cm (13.0 in.), a pair of discrete vortices exist, detached from the body surface. A fine sheet can be seen running from the separation line on the surface, feeding vorticity into the vortex. The photographs (fig. 8(b)) at  $x = 12.7$  cm (5.0 in.) and  $x = 22.9$  cm (9.0 in.) are typical of vapor screen photographs showing the initial formation of a discrete vortex with its feeder sheet. An example of a similar vortex formation is shown in figure 9 near the base of model B at  $\alpha = 20^\circ$  with  $M = 2.86$ .

When the angle of attack is increased, the vorticity increases and the discrete vortices above the body become stronger. As indicated in figure 8(b), the discrete vortices also become larger. As long as the flow is completely symmetric, the vertical plane through the axis acts as a reflection plane; consequently, the vortices cannot expand beyond the plane. They tend, therefore, to become elongated, as shown by the example in figure 10.

When  $\alpha$  is further increased, the vortex becomes even larger and eventually appears to fill virtually the entire area bounded by the body, the feeder sheet, the upper tip of the vortex, and the reflection plane, as in the example of figure 11.

Only relatively strong vortex effects could be detected by the schlieren system. For example, a rather diffuse line is shown emanating from the leeward surface in figure 12(a) at about the 20.3-cm (8.0 in.) station. The corresponding oil-flow photograph (fig. 12(b)) shows a weak separation line beginning near the shoulder, with strong vortex shedding beginning at  $x \approx 15.2$  cm (6.0 in.). For this case, the vapor-screen photographs (fig. 12(c)) show no vorticity at  $x = 12.7$  cm (5.0 in.), incipient vorticity at  $x = 22.9$  cm (9.0 in.), and discrete vortices at the 33.0-cm (13.0 in.) station.

A survey of the oil-flow photographs indicates that, with the ranges of  $M$  and  $\alpha$  studied, a considerable distance is required for the flow to adjust to the uniform geometry of the afterbody. In fact, a uniform flow was not established over any significant part of the body during most of the study. This effect is readily observed in the oil-flow photographs of model B. The oil-flow patterns on model B at  $M = 2.16$  for  $\alpha = 15^\circ$ ,  $20^\circ$ , and  $30^\circ$  are shown in figure 13. These flow photographs indicate that, at the higher angles, a uniform pattern exists over no more than 20 percent of the body near the base. The corresponding photographs for model A (fig. 14) display similar characteristics, but the primary separation line forms farther forward than on model B.

### Summary

Several characteristics of these surface flows differ from the theoretical flow model that has been used for high angles of attack (ref. 5) and from the linear inviscid model that is applicable at low angles of attack. First, separation at these moderate angles of attack does not begin at the  $180^\circ$  meridian as described in reference 5 for missiles at high angles of attack. Even on the body of revolution at  $\alpha = 30^\circ$ , the separation line begins at an angular displacement of approximately  $20^\circ$  to  $30^\circ$  from the  $180^\circ$  meridian, and at lower angles, the displacement is even greater (fig. 14). This result appears reasonable from a theoretical viewpoint. At the minimum angle of attack at which separation occurs, the separation should probably begin slightly aft of the shoulder and above the  $90^\circ$  meridian line. Here, the cross-flow component encounters an adverse pressure gradient, as shown in figure 3(a). Simultaneously, the axial-flow component encounters a slight adverse gradient behind the shoulder, as shown in figure 15, for which the calculation was performed by the method of reference 6. It then appears reasonable that, as the angle of attack is increased above this minimum, the initial separation points would move forward and upward, as is actually indicated by the oil-flow photographs (figs. 13 and 14).

A second characteristic difference of these surface flows is that the streamlines immediately behind the shoulder sweep downward across the meridian lines, even when

no distinct separation line is apparant. (See oil-flow photographs of figs. 13 and 14.) This behavior, however, is inconsistent with an attached-flow model for which the surface streamlines always have a positive slope relative to the meridian lines.

A third characteristic difference is that at the lower angles of attack strong vortex effects do not appear immediately behind the shoulder, but some distance back on the afterbody. These characteristics are indicative of a rather complex flow pattern near and aft of the shoulder. Since the initial separation point is displaced from the  $180^{\circ}$  meridian, the surface flow above the separation line is still attached, at least for some distance along the afterbody. The vorticity generated in the field above the body by the separating streamlines is relatively weak initially and is not visible in the vapor screen or schlieren photographs. Although weak, this field vorticity induces a downward component of velocity on the surface, causing the leeward surface flow to sweep downward across the meridian lines and increasing the adverse cross-flow pressure gradient. Consequently, the separation line moves downward toward the  $90^{\circ}$  meridian (and even below it sometimes), resulting in an increase in the strength of the separation vortex.

Thus, the separation process is cumulative. The separation vortex eventually becomes large and strong enough to scrub the surface thoroughly, producing the dark bands in the oil-flow photographs. These strong vortices are also visible in the schlieren photographs. Once these strong vortex effects appear and the separation line becomes nearly straight, the surface flow pattern approaches some uniformity. Initial-separation, reattachment, and secondary-separation lines can be distinguished in the oil-flow photographs for some of the runs.

For model C, the flow considerations are similar to those for the other models, but the pattern is more complicated because of the geometry. Primary and secondary separation lines appear on the semicylindrical part of the afterbody and on the "canopy" part, resulting in a maze of lines that would be difficult to decipher in detail (fig. 16).

## CONCLUDING REMARKS

Three missile body shapes were tested at supersonic Mach numbers (1.50, 2.16, and 2.86) and moderate angles of attack (up to  $30^{\circ}$ ). At the test Reynolds number of  $8.2 \times 10^6/\text{m}$  ( $2.5 \times 10^6/\text{ft}$ ), laminar flow on the models without transition grit gave rise to asymmetric vortex shedding. This effect was virtually eliminated by the addition of transition grit to the models.

The normal-force coefficients for the two shaped bodies were lower than for the body of revolution. The normal force due to cross-flow drag was larger than the values computed by a semiempirical theory. With the moment center taken slightly aft of the shoulder, the pitching-moment variation was a sensitive indicator of incipient separation.

The design of a cross-section shape to ease the adverse cross-flow pressure gradient appeared to be ineffective in delaying separation to an extent sufficient to influence the normal force significantly. The cross-flow drag appeared to be primarily a function of cross-flow fineness ratio.

At moderate angles of attack, the flow does not attain a uniform pattern over the major part of the afterbody. Incipient separation, which is not readily observable in the flow visualization photographs, apparently gives rise to weak vorticity in the field above the surface. This vorticity then interacts with the surface flow in a cumulative manner to cause stronger vortex effects, which are easily seen in the flow visualization photographs.

Langley Research Center  
National Aeronautics and Space Administration  
Hampton, VA 23665  
November 13, 1979

#### REFERENCES

1. Thomson, K. D.; and Morrison, D. F.: The Spacing, Position and Strength of Vortices in the Wake of Slender Cylindrical Bodies at Large Incidence. Rep. HSA 25, Weapons Res. Establ., Australian Def. Sci. Serv., June 1969.
2. Carlson, Harry W.; and Gapcynski, John P.: An Experimental Investigation at a Mach Number of 2.01 of the Effects of Body Cross-Section Shape on the Aerodynamic Characteristics of Bodies and Wing-Body Combinations. NACA RM L55E23, 1955.
3. Monta, William J.: Supersonic Aerodynamic Characteristics of a Sparrow III Type Missile Model With Wing Controls and Comparison With Existing Tail-Control Results. NASA TP-1078, 1977.
4. Nielsen, Jack N.: Missile Aerodynamics. McGraw-Hill Book Co., Inc., 1960.
5. Thomson, K. D.: The Estimation of Viscous Normal Force, Pitching Moment, Side Force and Yawing Moment on Bodies of Revolution at Incidences up to  $90^{\circ}$ . WRE-Rep.-782 (WR&D), Australian Def. Sci. Serv., Oct. 1972.
6. Marconi, Frank; Salas, Manuel; and Yaeger, Larry: Development of a Computer Code for Calculating the Steady Super/Hypersonic Inviscid Flow Around Real Configurations. Volume I - Computational Technique. NASA CR-2675, 1976.

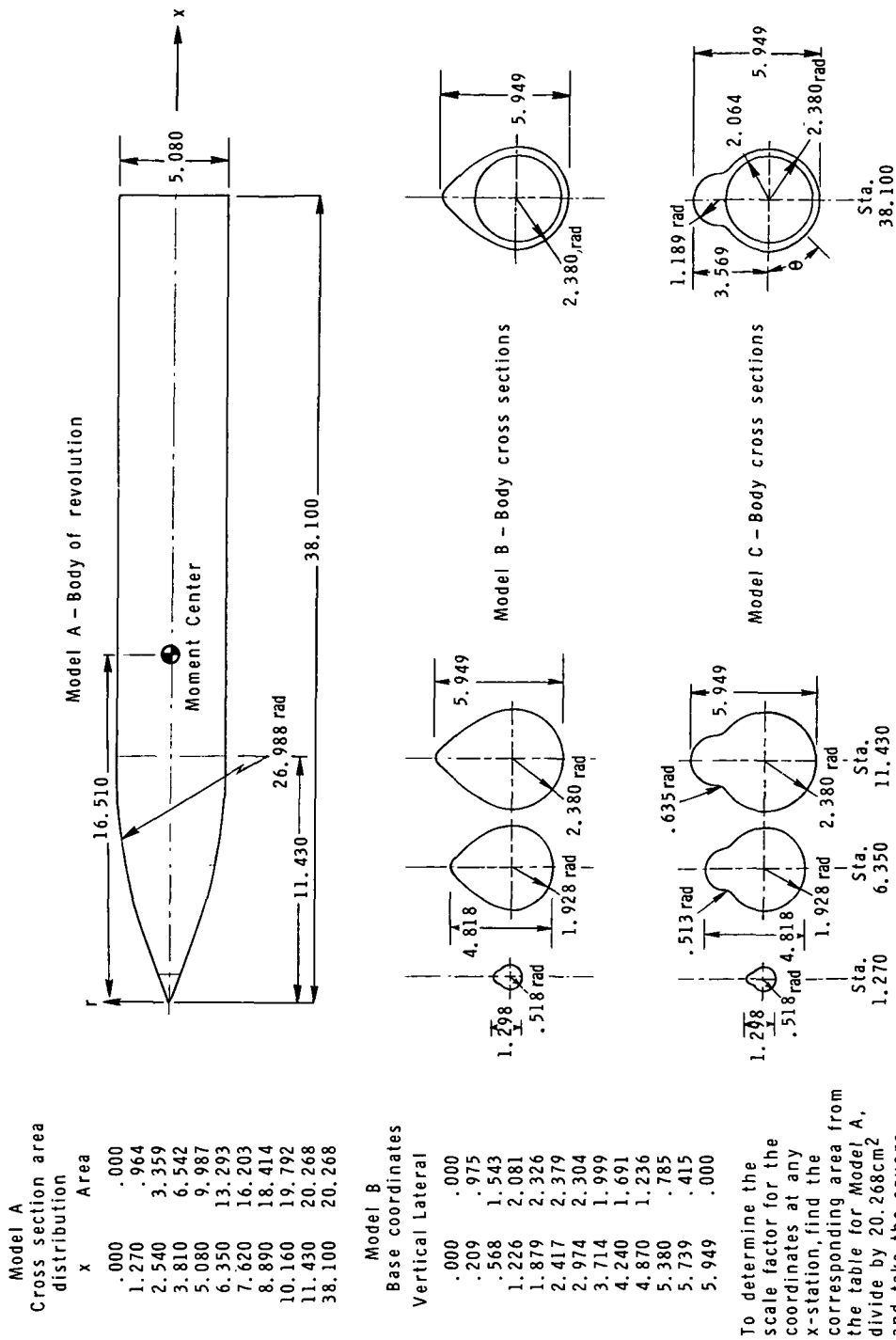
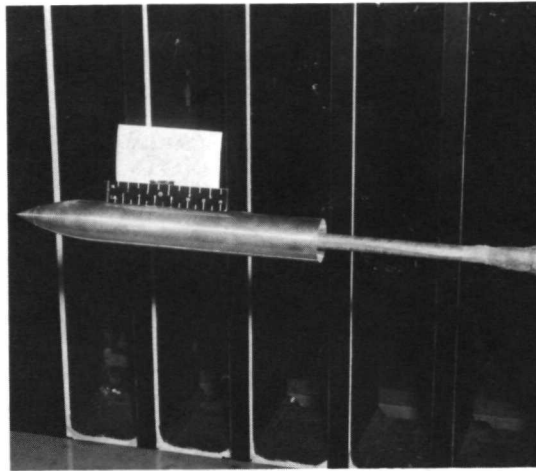
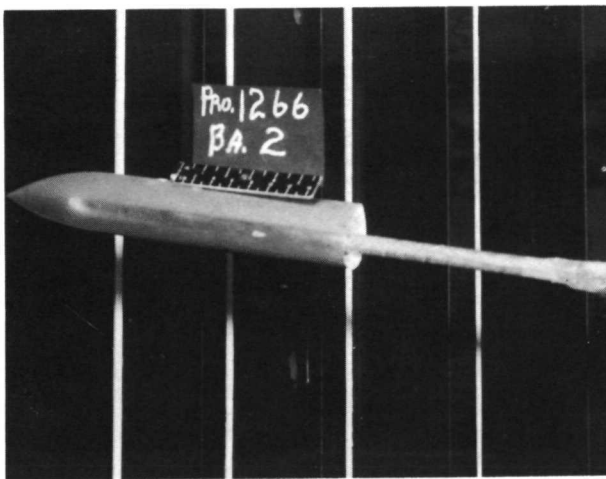


Figure 1.- Model geometry. (All model dimensions in cm.)

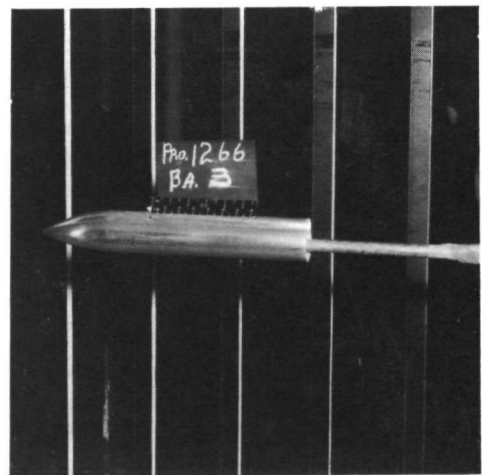




Model A



Model B



Model C

Figure 2.- Photographs of models.

L-79-319

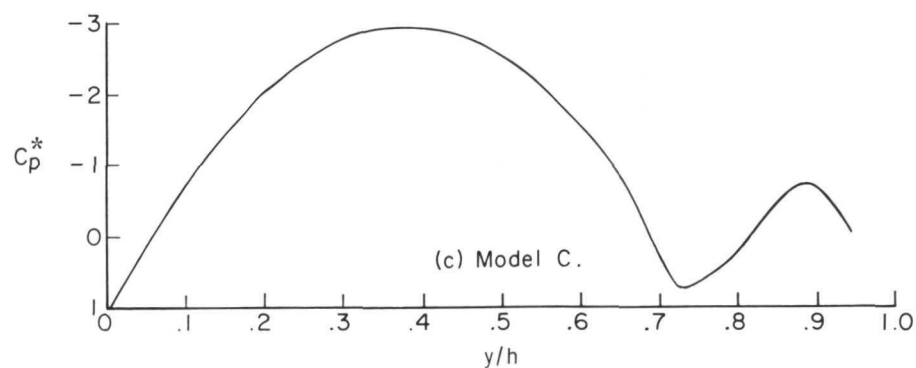
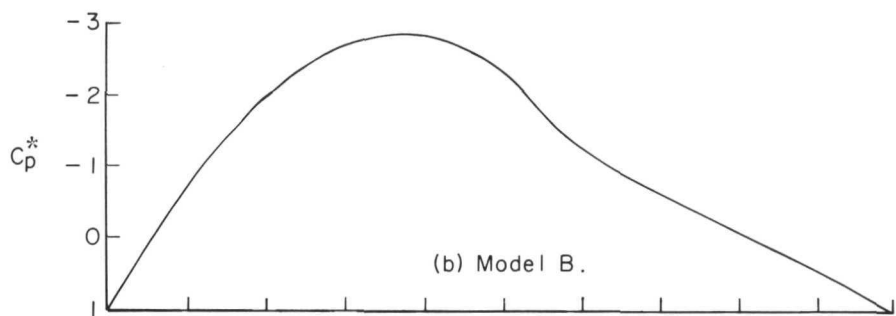
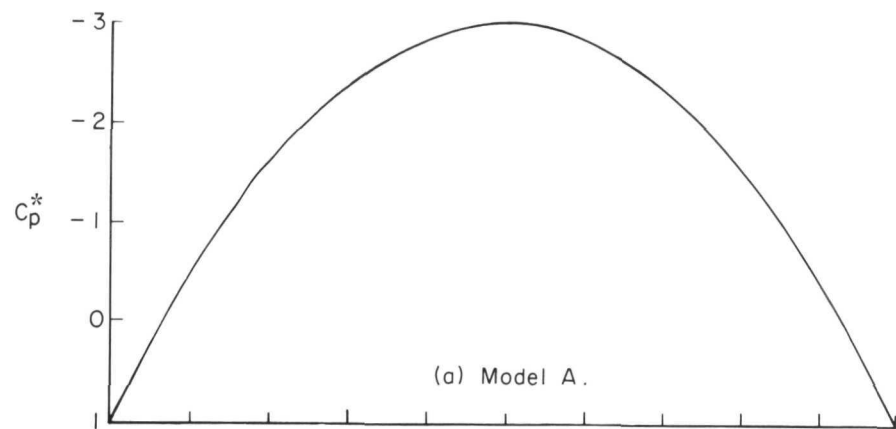
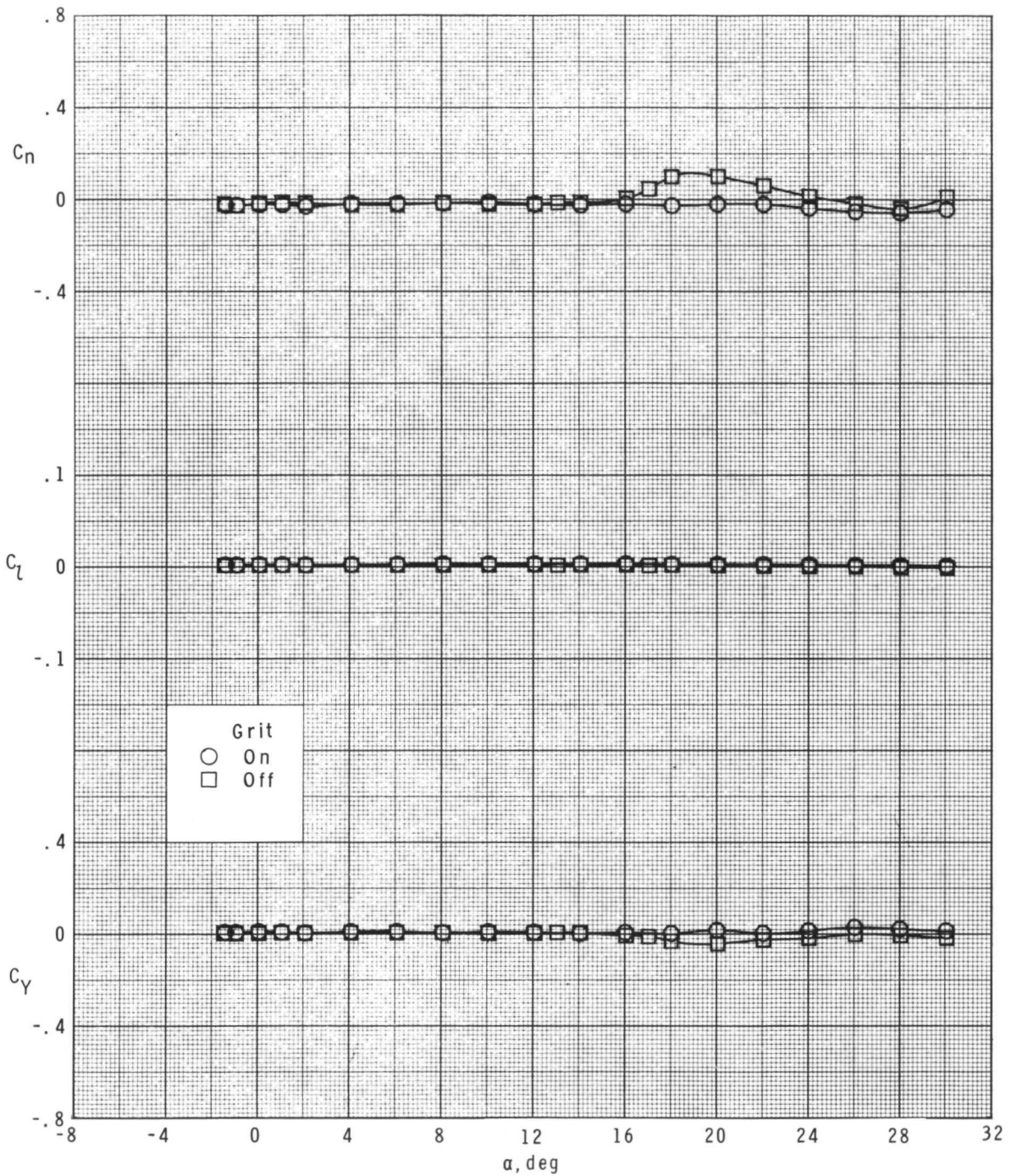
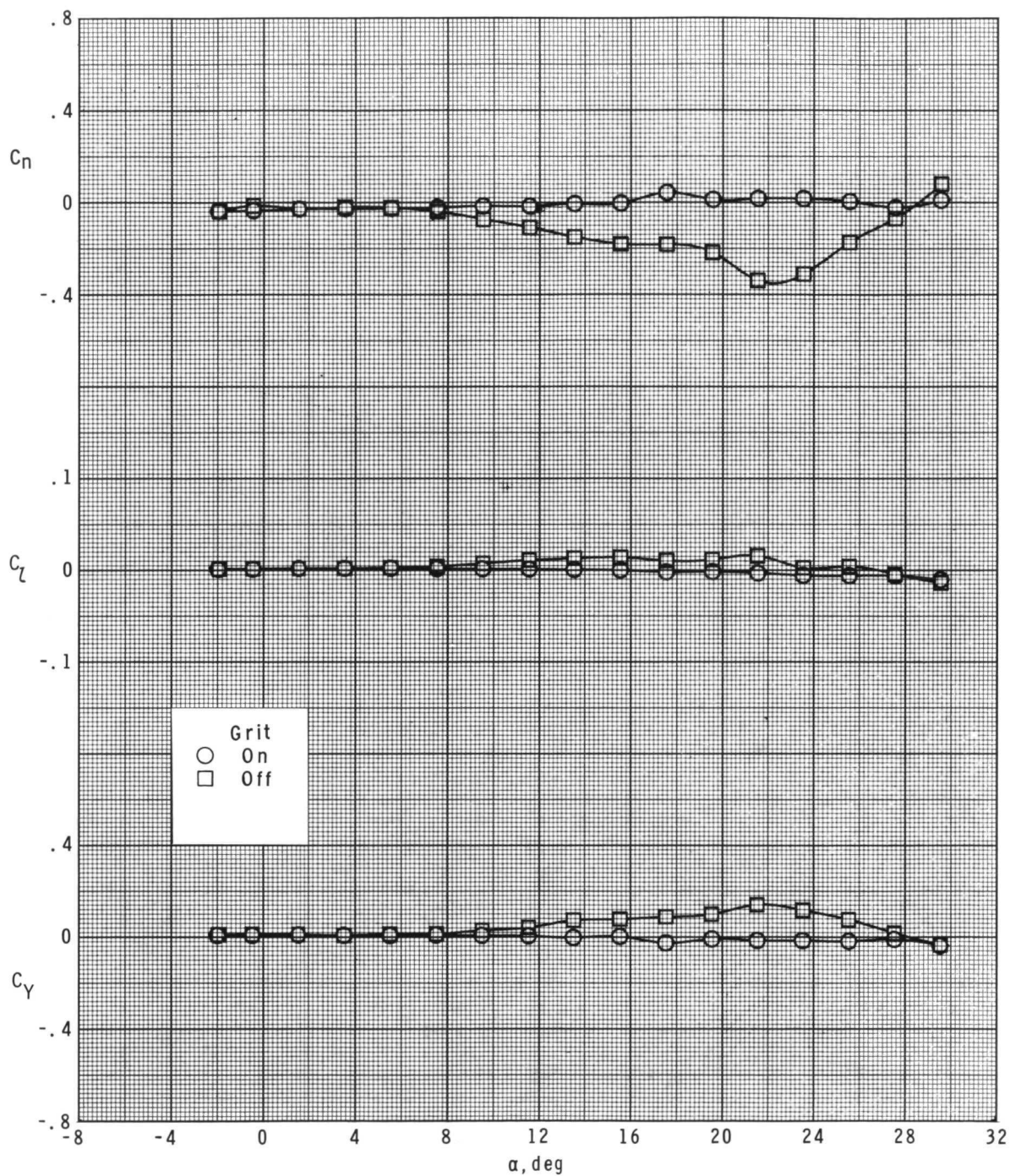


Figure 3.- Theoretically determined cross-flow pressure distributions for models A, B, and C.



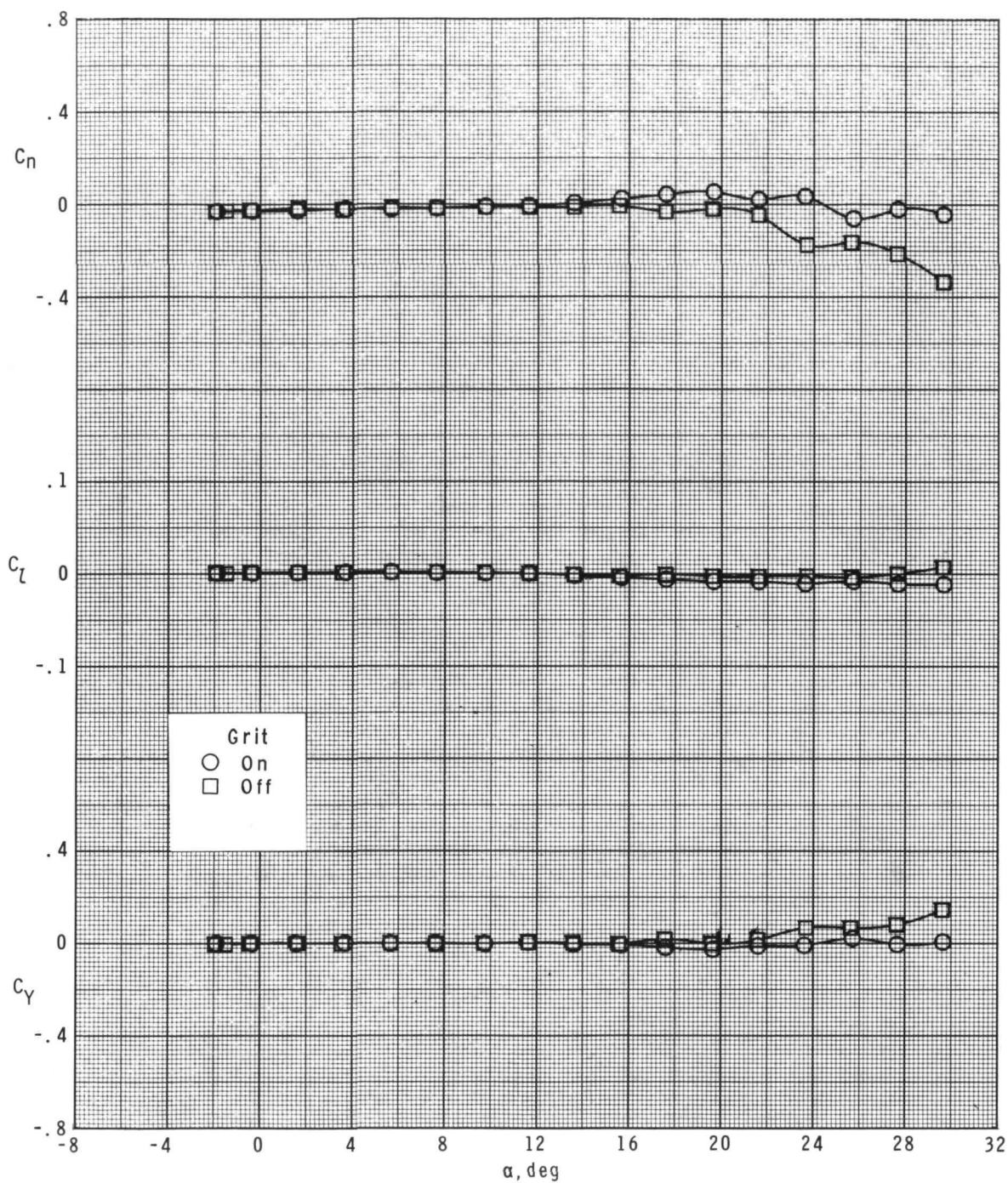
(a) Model A.

Figure 4.- Effect of grit on lateral aerodynamic characteristics  
at  $M = 1.50$  with  $\beta = 0^\circ$ .



(b) Model B.

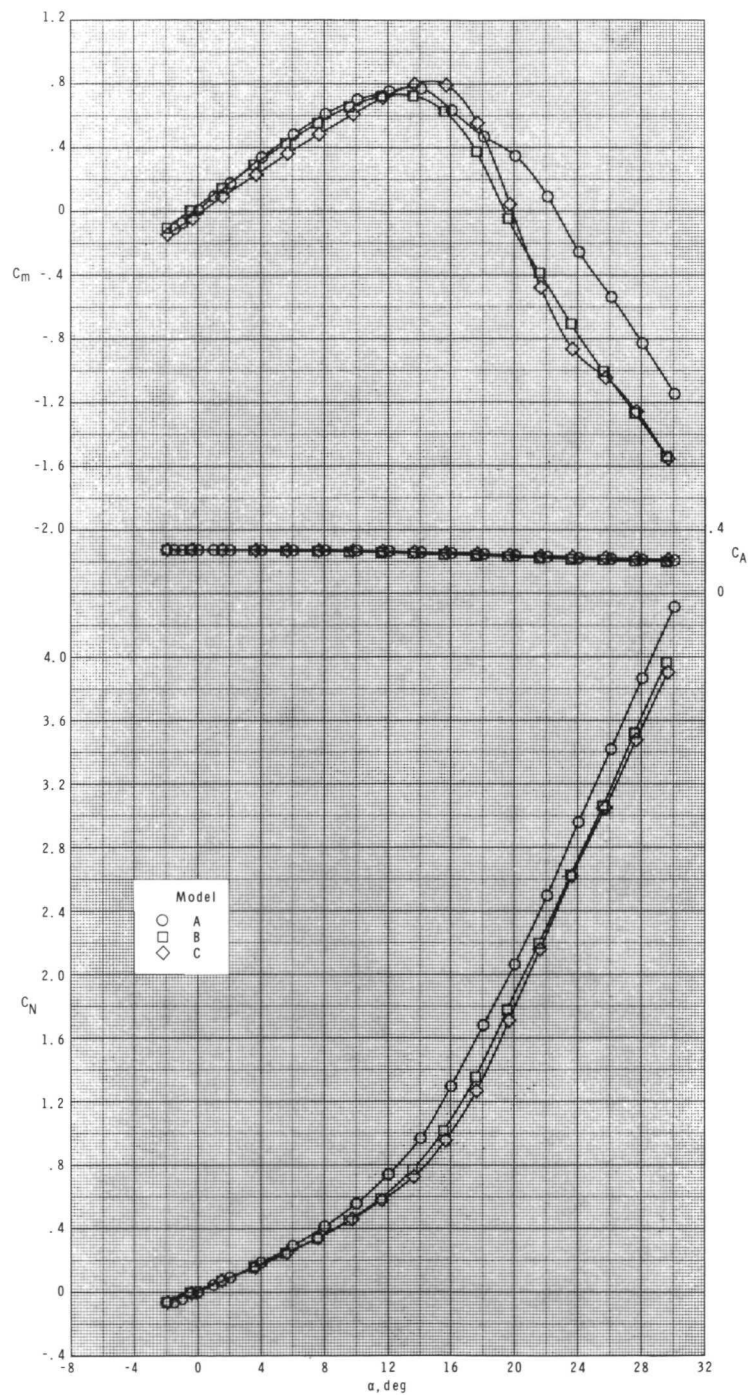
Figure 4.- Continued.



(c) Model C.

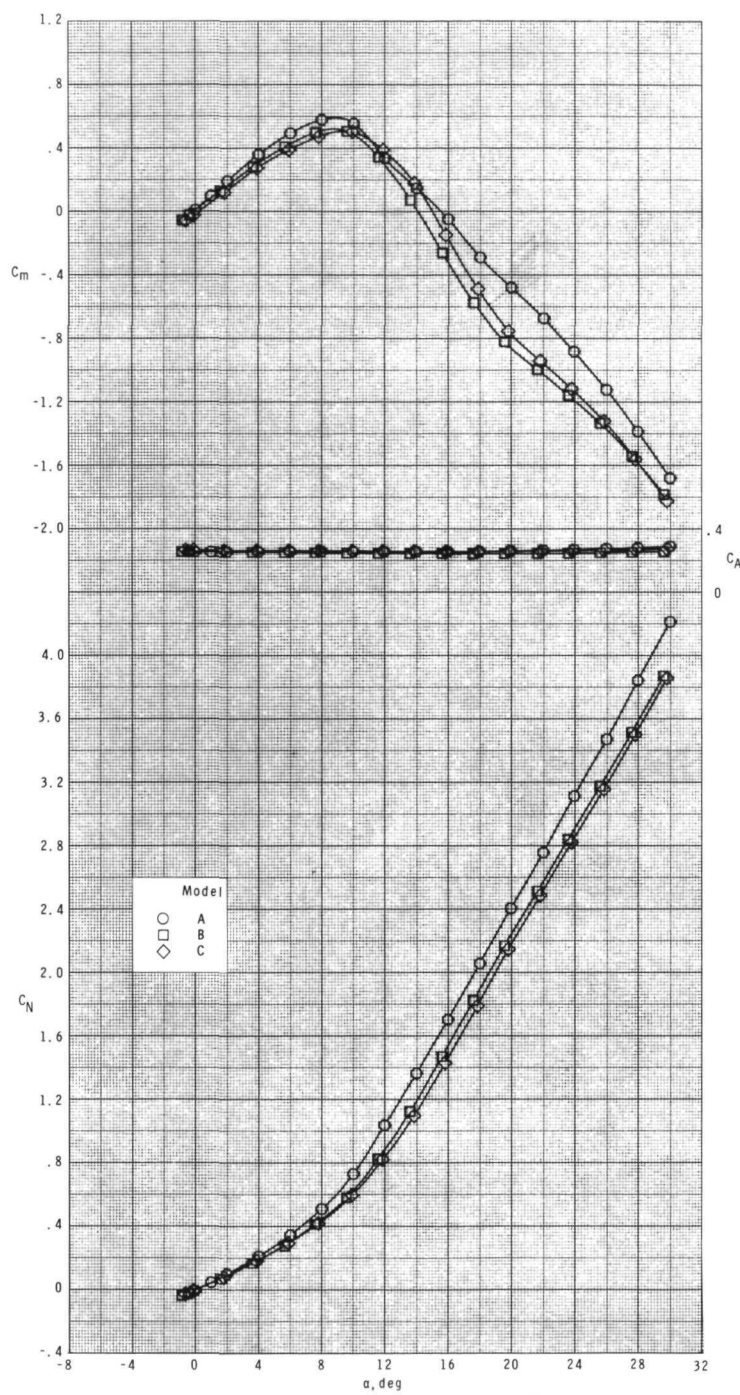
Figure 4.- Concluded.





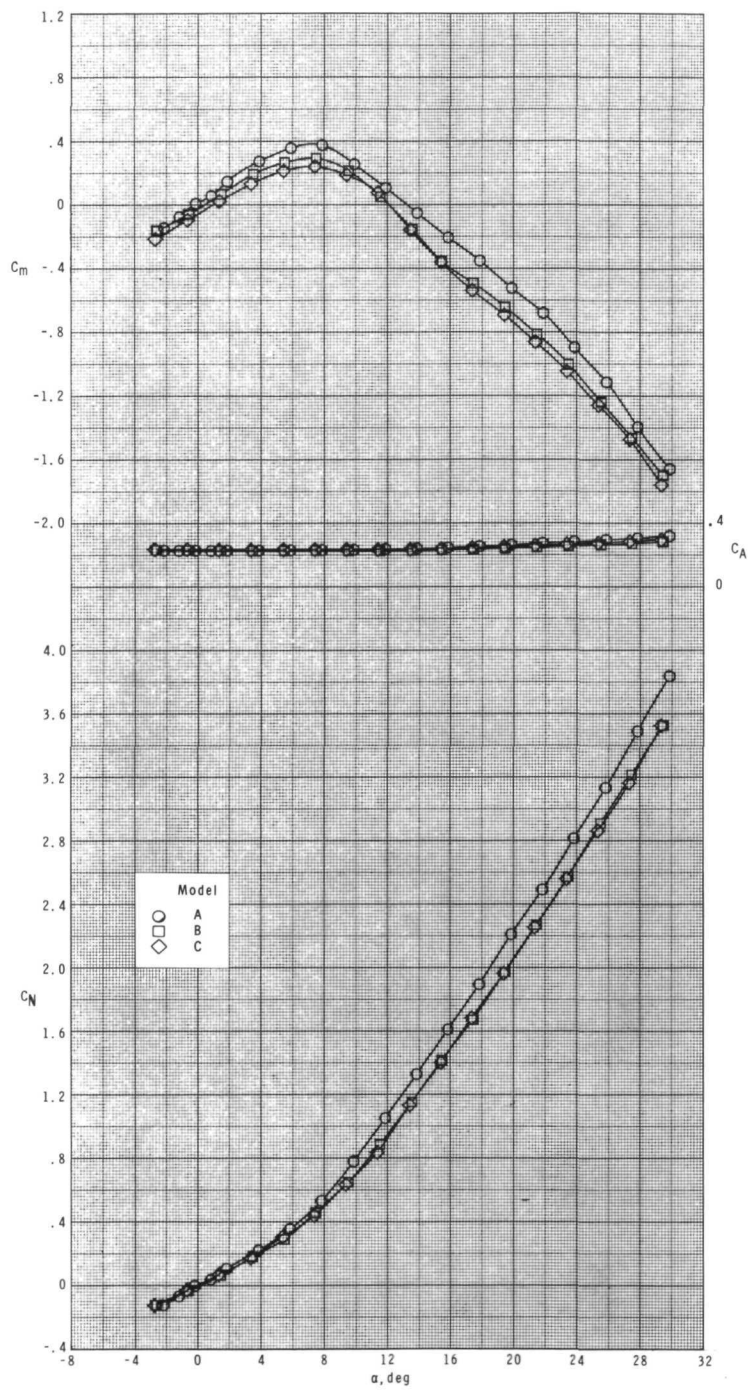
(a)  $M = 1.50$ .

Figure 5.- Pitching-moment, axial-force, and normal-force coefficient variations with angle of attack.



(b)  $M = 2.16$ .

Figure 5.- Continued.



(c)  $M = 2.86$ .

Figure 5.- Concluded.



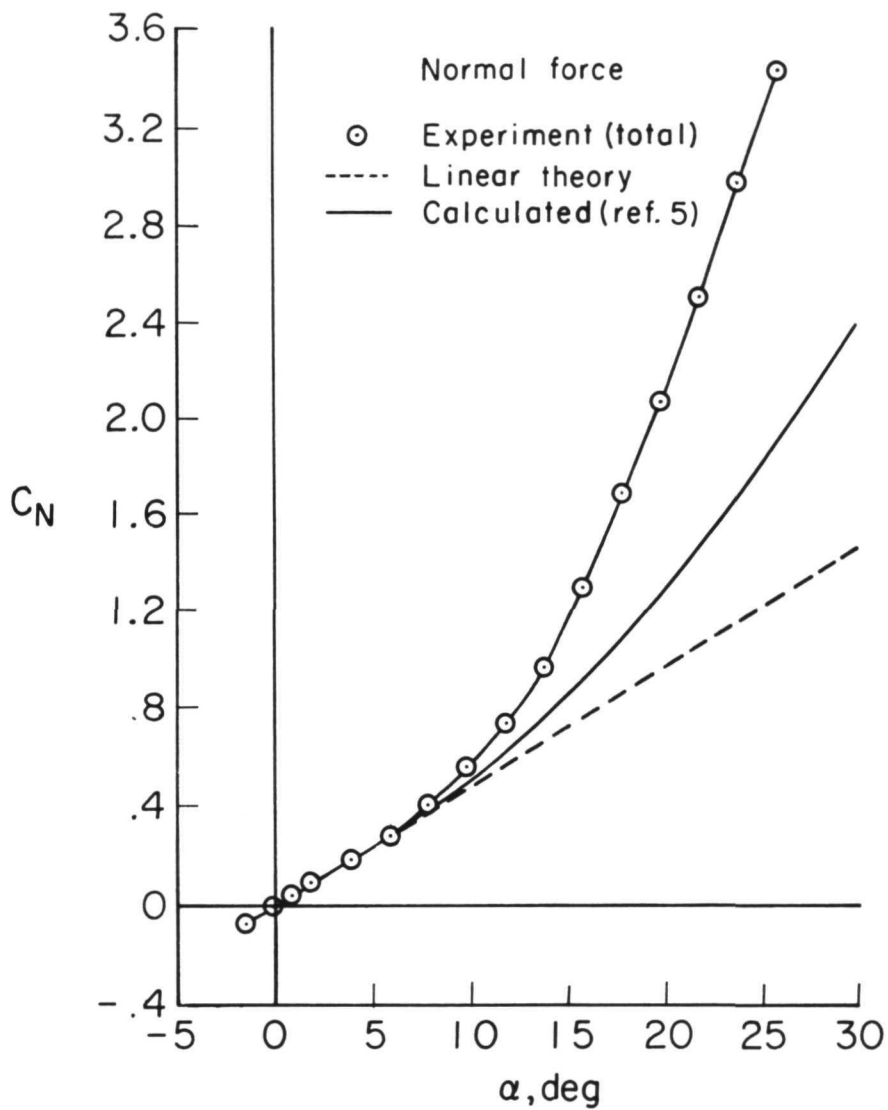
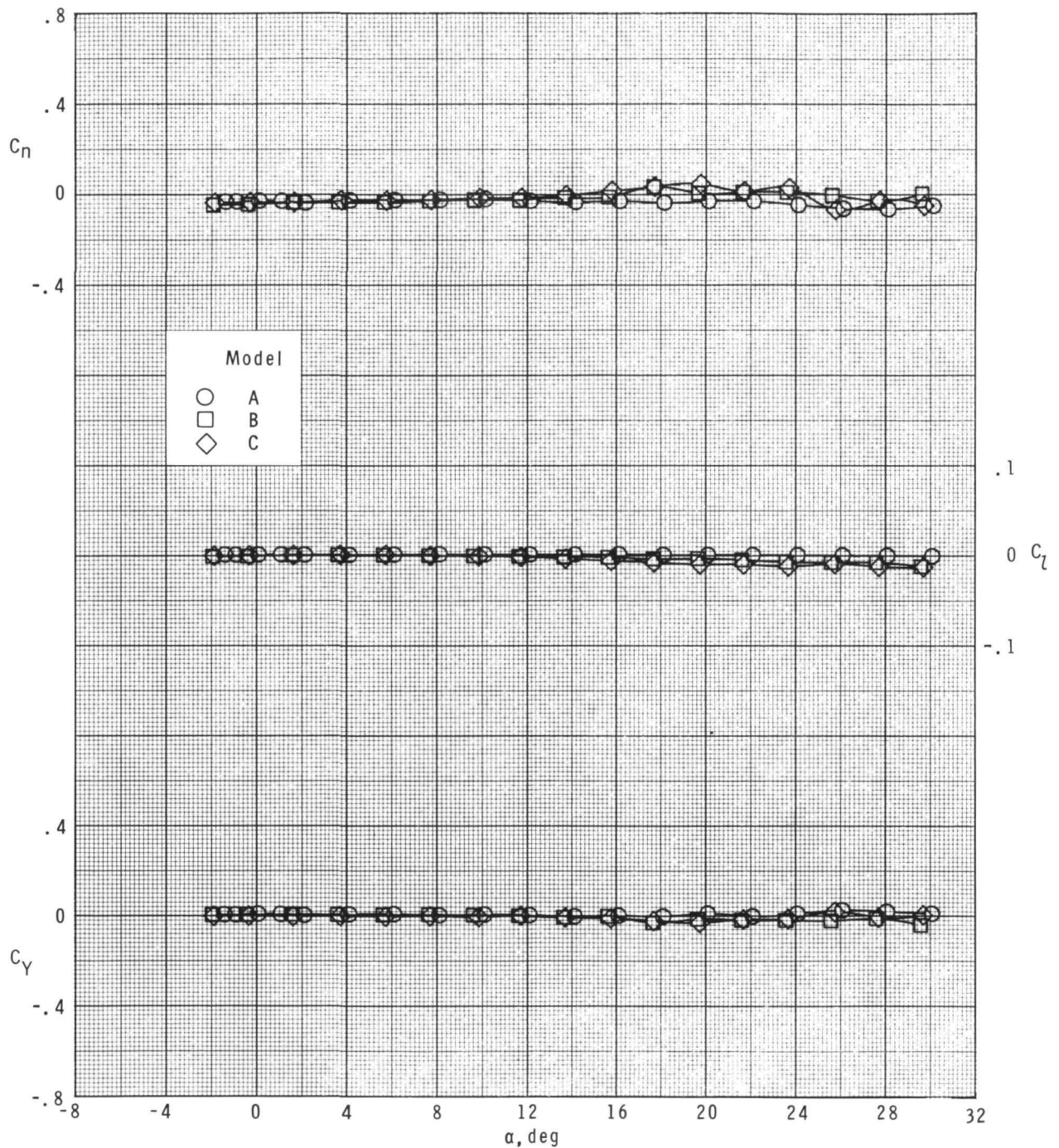
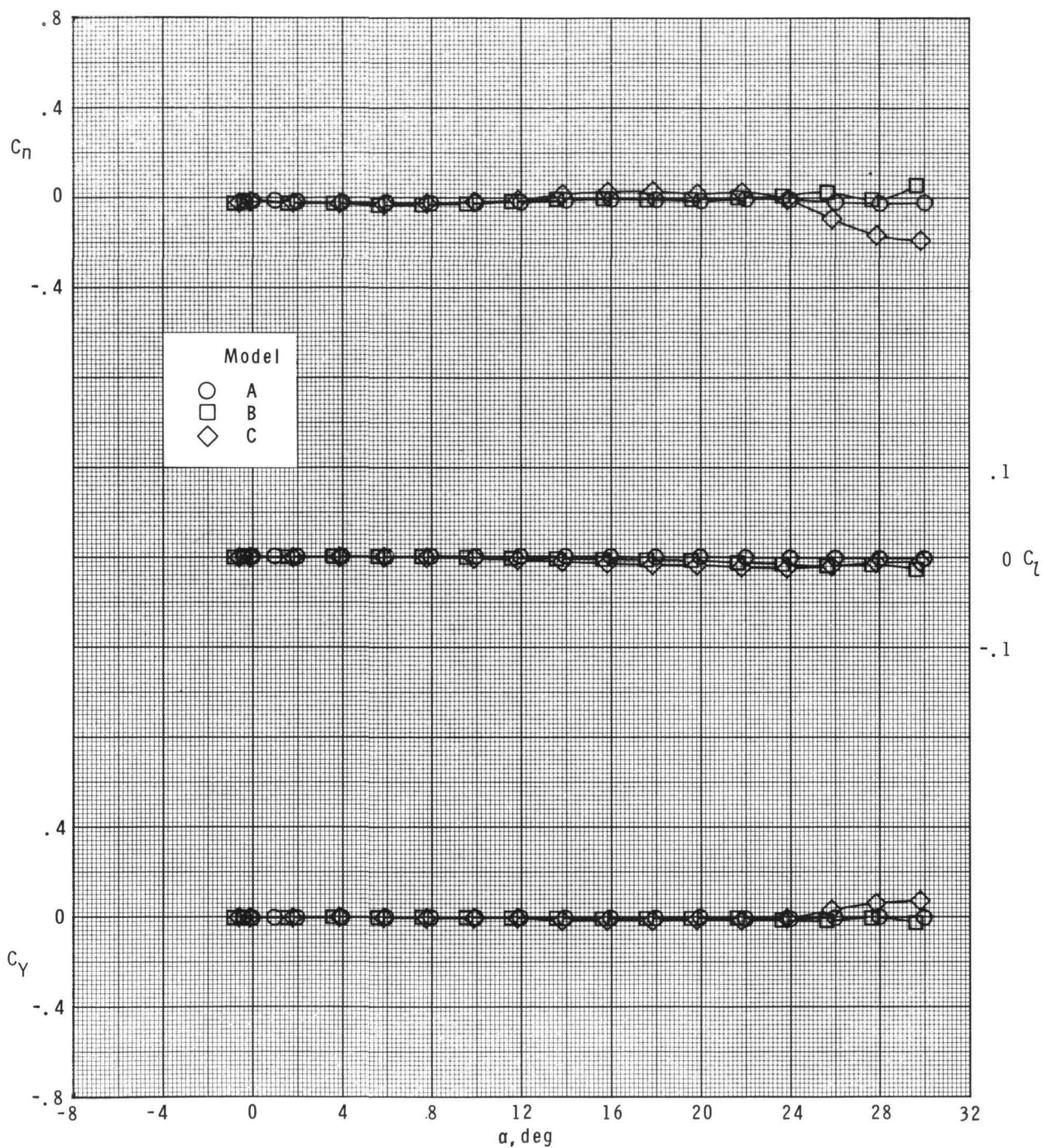


Figure 6.- Comparison of experimental and theoretical values of normal-force drag due to separation on model A at  $M = 1.50$ .



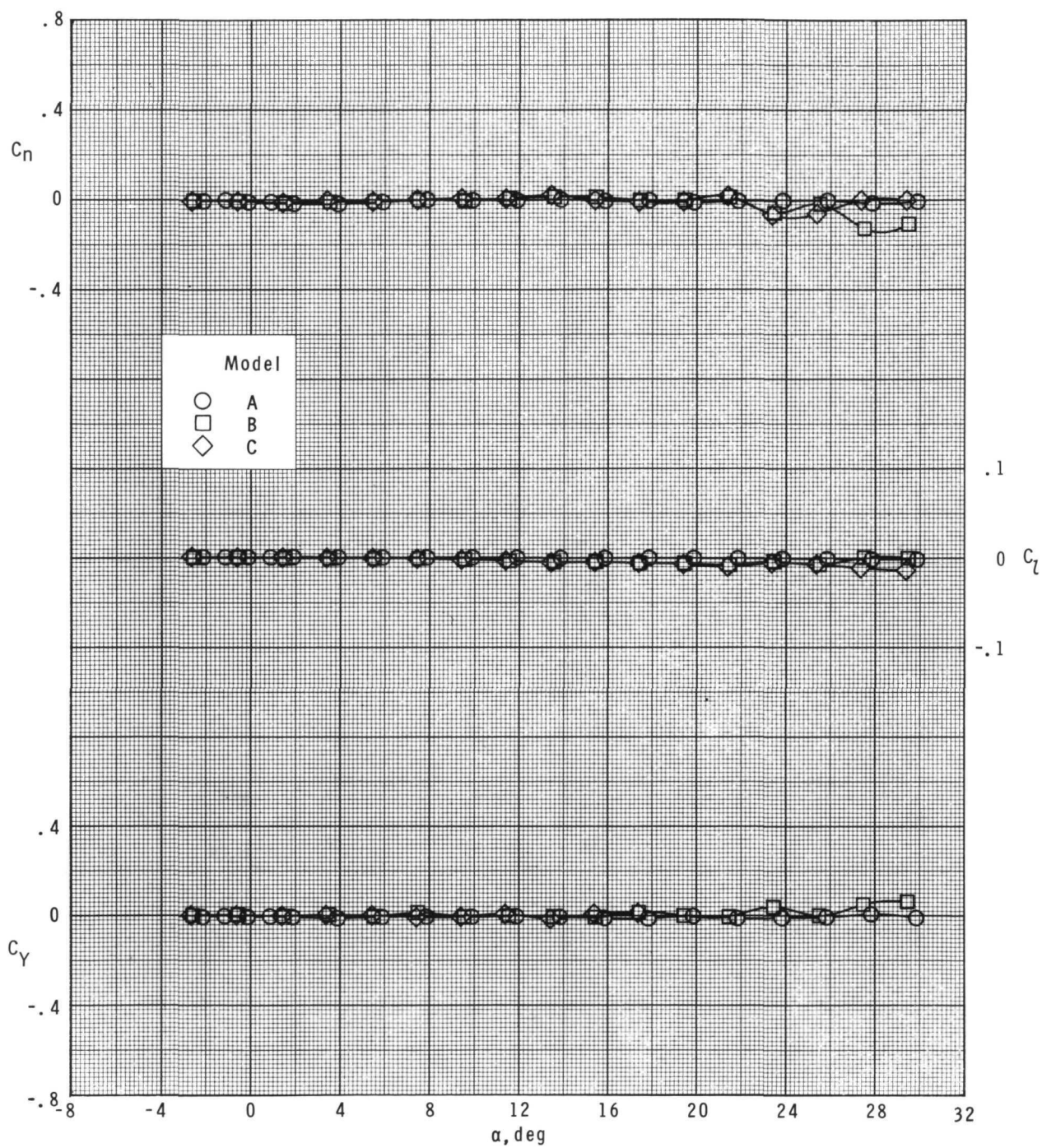
(a)  $M = 1.50$ .

Figure 7.- Lateral aerodynamic characteristics for models A, B, and C  
at  $M = 1.50, 2.16, \text{ and } 2.86$  with  $\beta = 3^\circ$ .



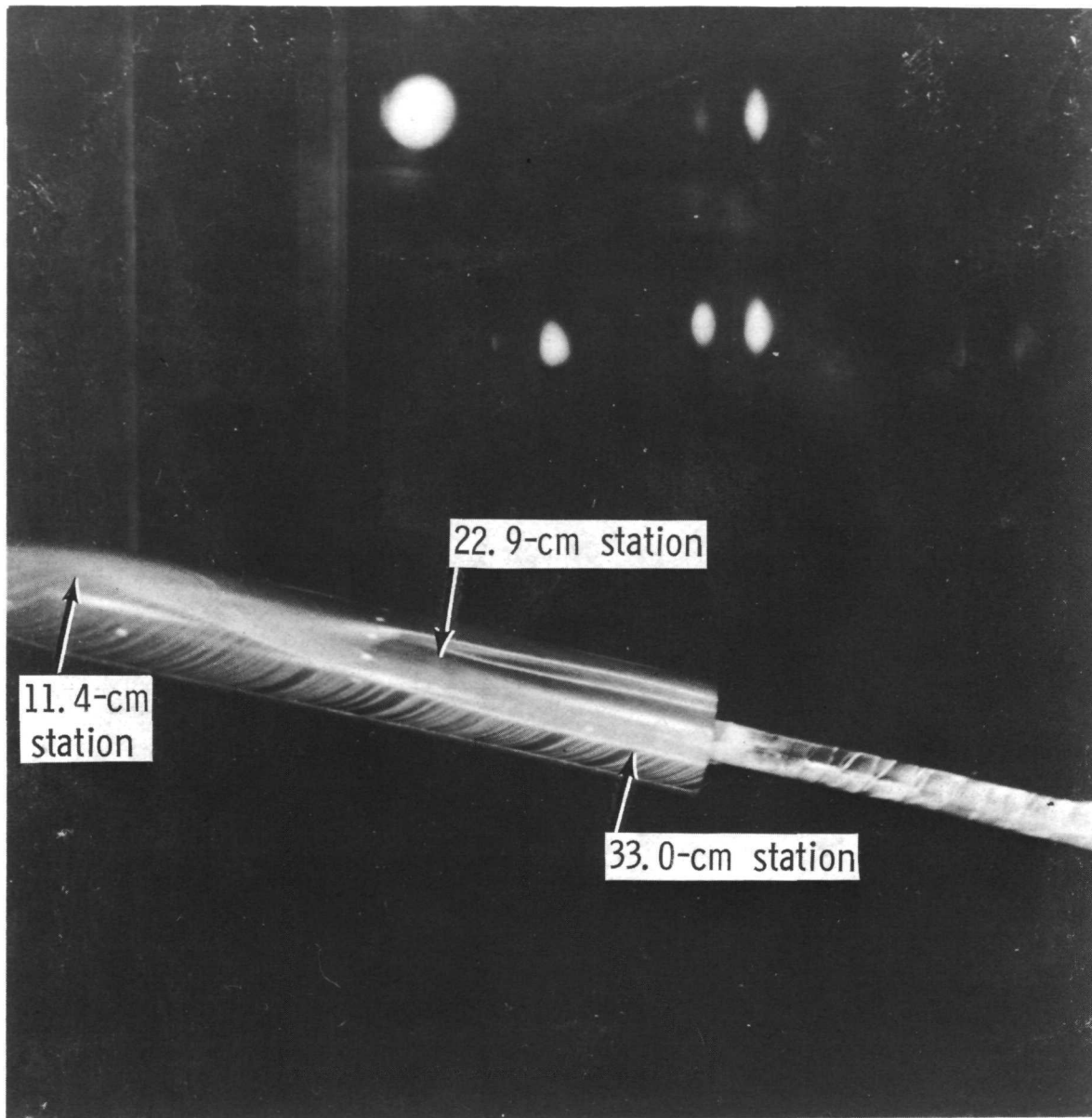
(b)  $M = 2.16$ .

Figure 7.- Continued.



(c)  $M = 2.86$ .

Figure 7.- Concluded.

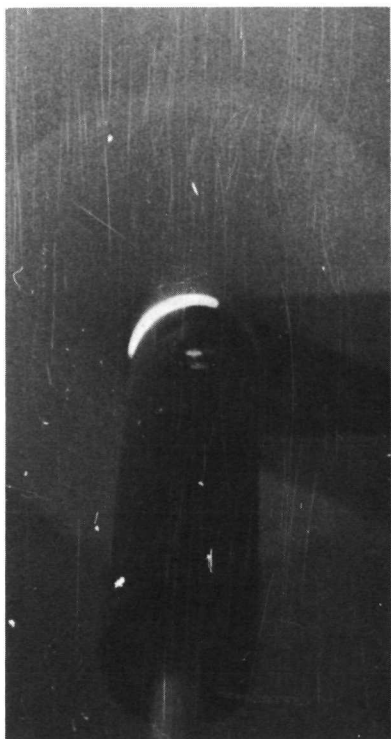


L-79-320

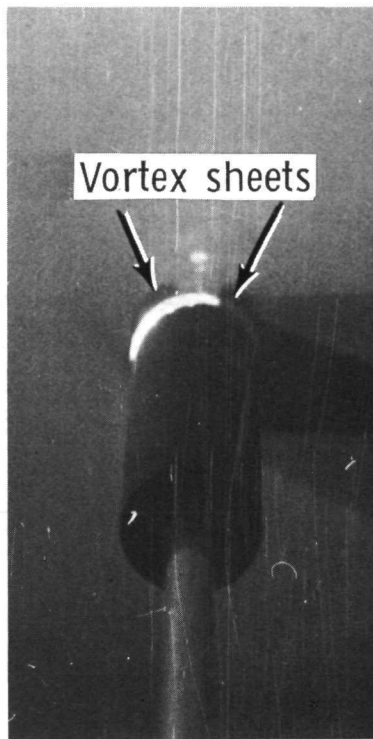
(a) Oil flow.

Figure 8.- Flow visualization photographs for model A  
at  $M = 2.16$  with  $\alpha = 15^\circ$ .





$x=12.7$  cm (5.0 in.)



$x=22.9$  cm (9.0 in.)

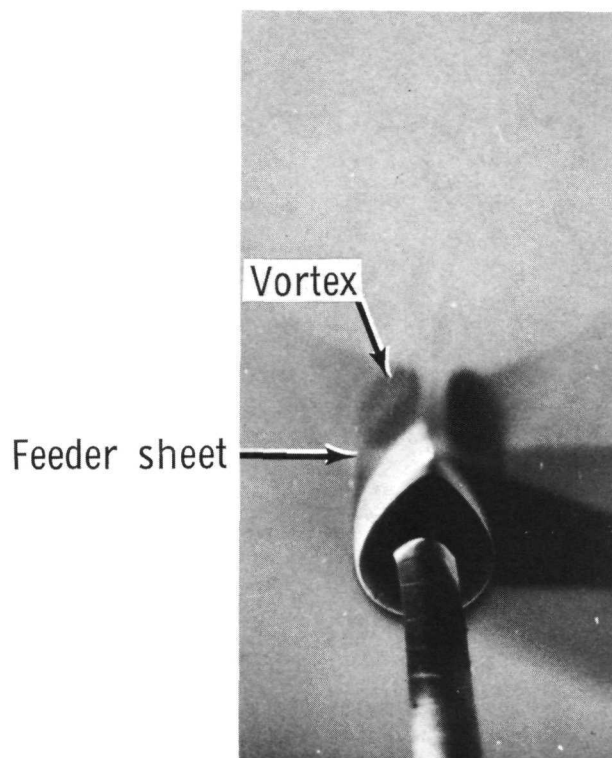


$x=33.0$  cm (13.0 in.)

(b) Vapor screen.

L-79-321

Figure 8.- Concluded.



L-79-322

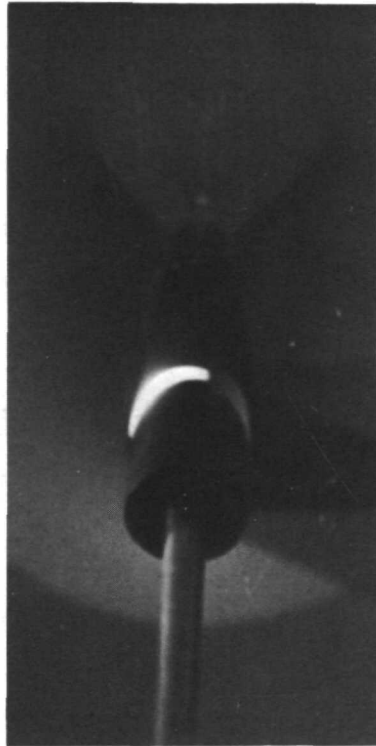
Figure 9.- Vapor-screen photograph near base of model B  
at  $M = 2.86$  with  $\alpha = 20^\circ$ .



L-79-323

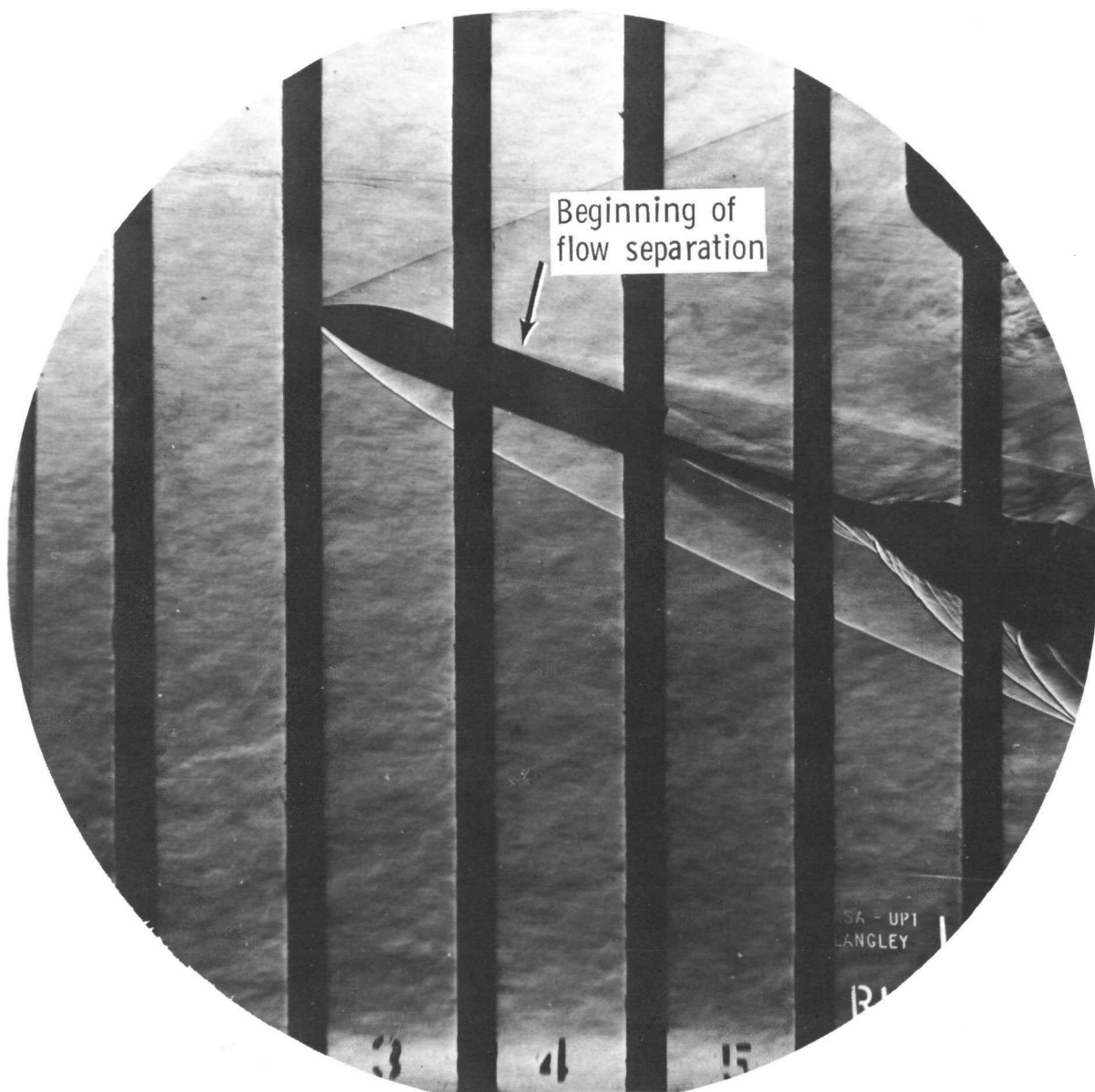
Figure 10.- Vapor-screen photograph of model A  
at  $x = 33.0$  cm (13.0 in.) with  $M = 2.86$  and  
 $\alpha = 20^\circ$ .





L-79-324

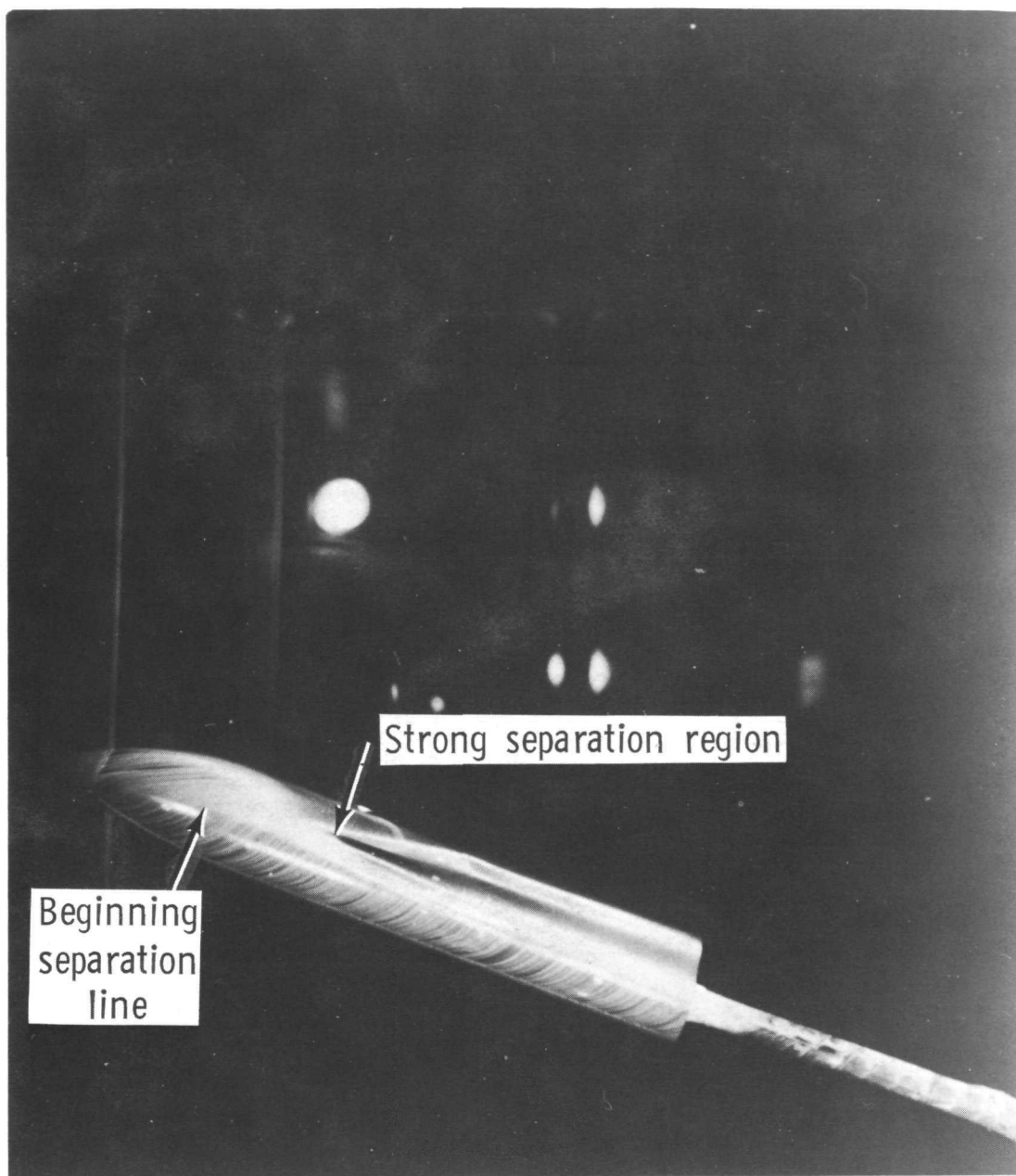
Figure 11.- Vapor-screen photograph of model A  
at  $x = 33.0$  cm (13.0 in.) with  $M = 2.86$  and  
 $\alpha = 30^\circ$ .



L-79-325

(a) Schlieren.

Figure 12.- Flow visualization photographs of model B  
at  $M = 2.86$  with  $\alpha = 20^\circ$ .



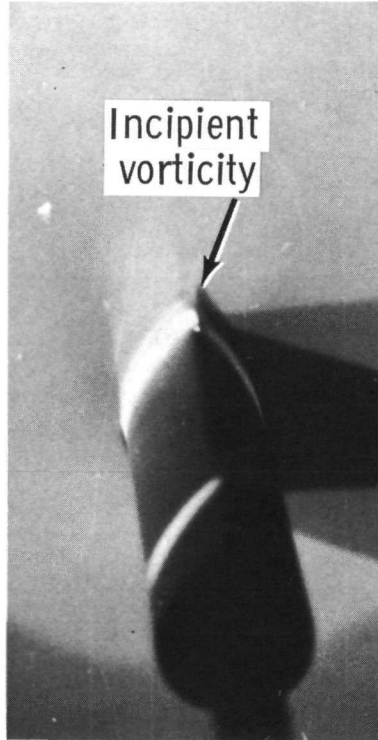
L-79-326

(b) Oil flow.

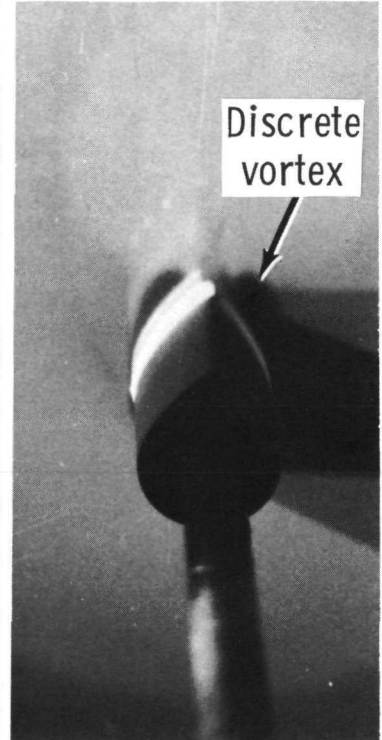
Figure 12.- Continued.



$x=12.7$  cm (5.0 in.)



$x=22.9$  cm (9.0 in.)

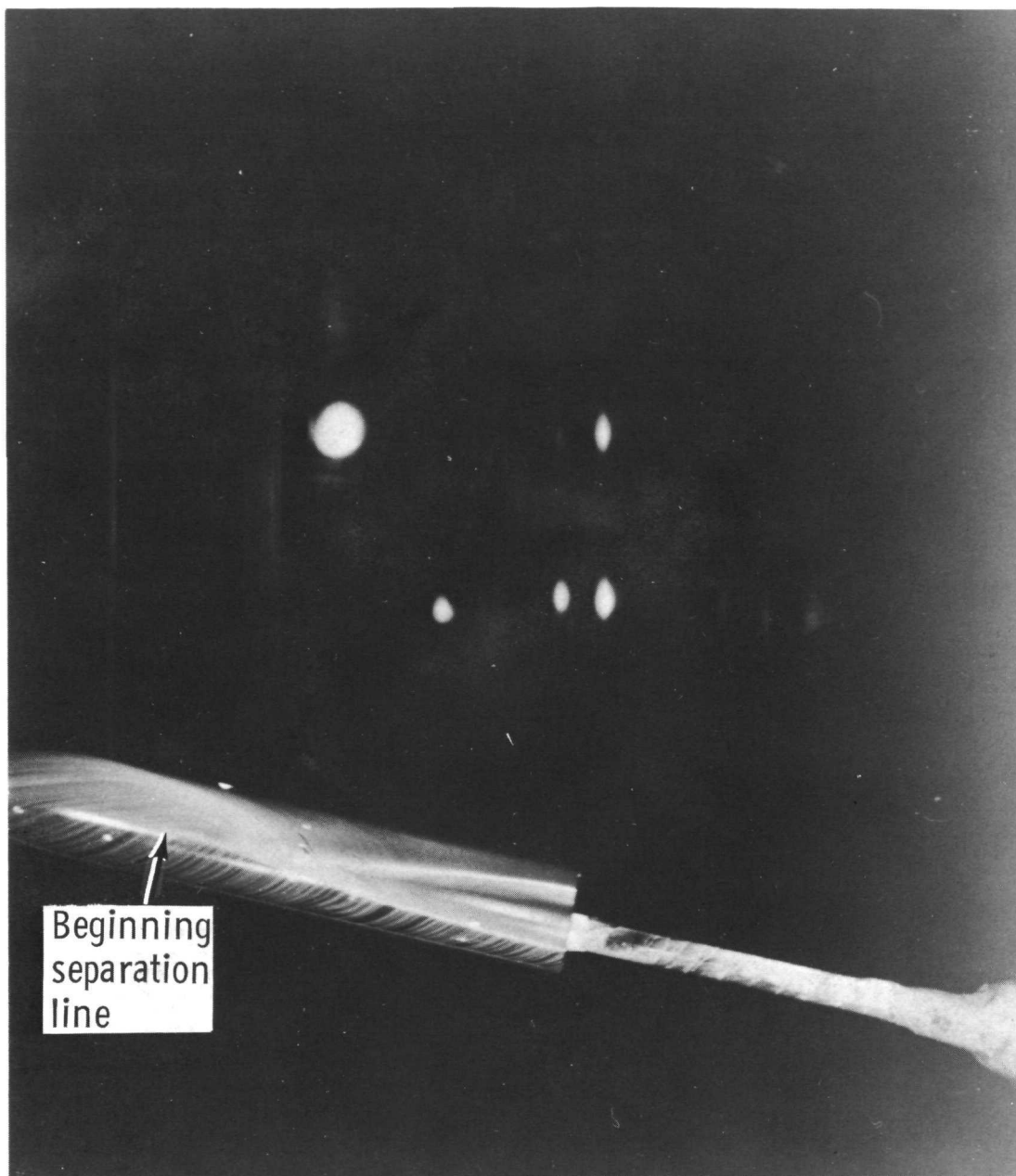


$x=33.0$  cm (13.0 in.)

(c) Vapor screen.

L-79-327

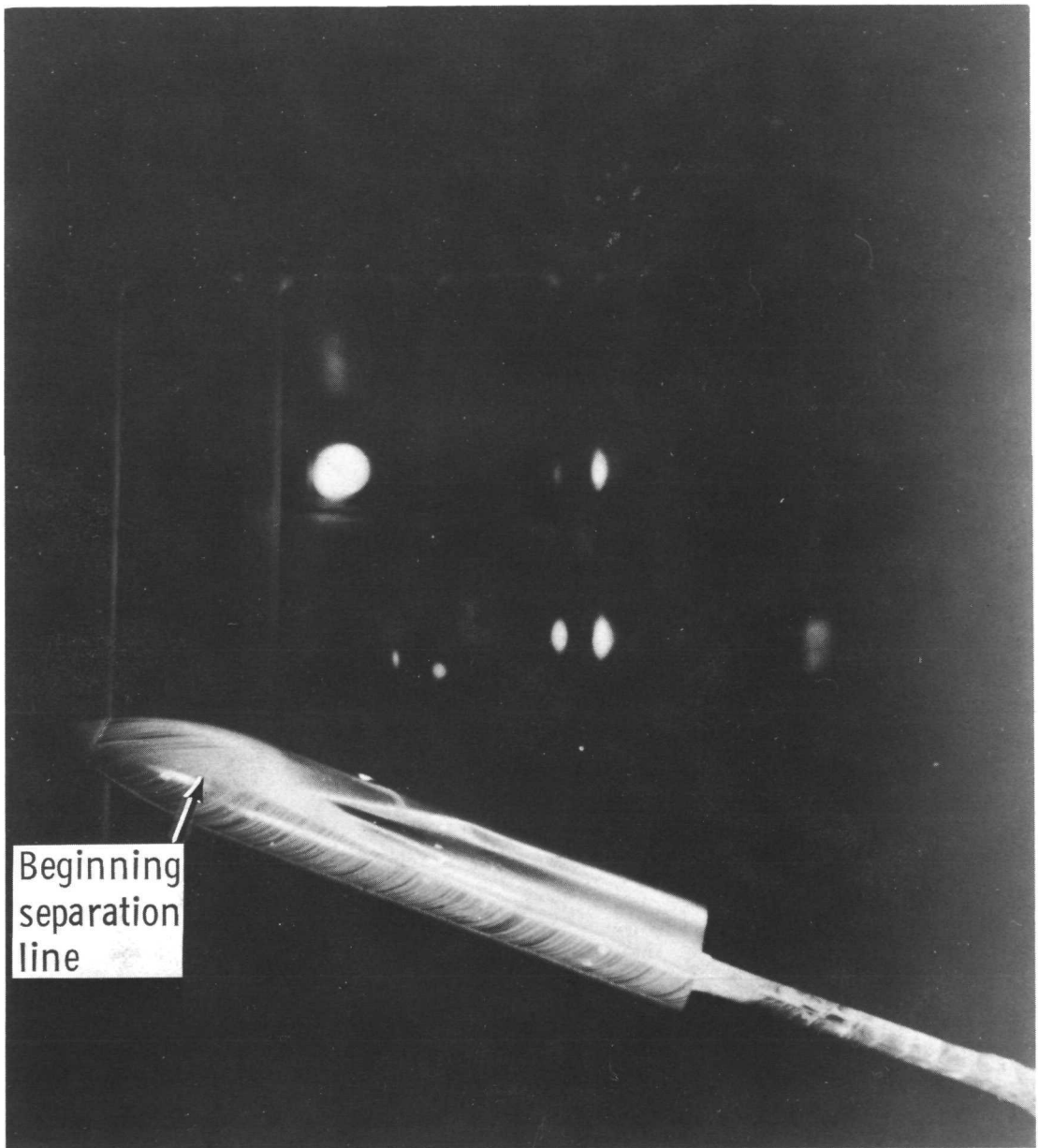
Figure 12.- Concluded.



(a)  $\alpha = 15^\circ$ .

L-79-328

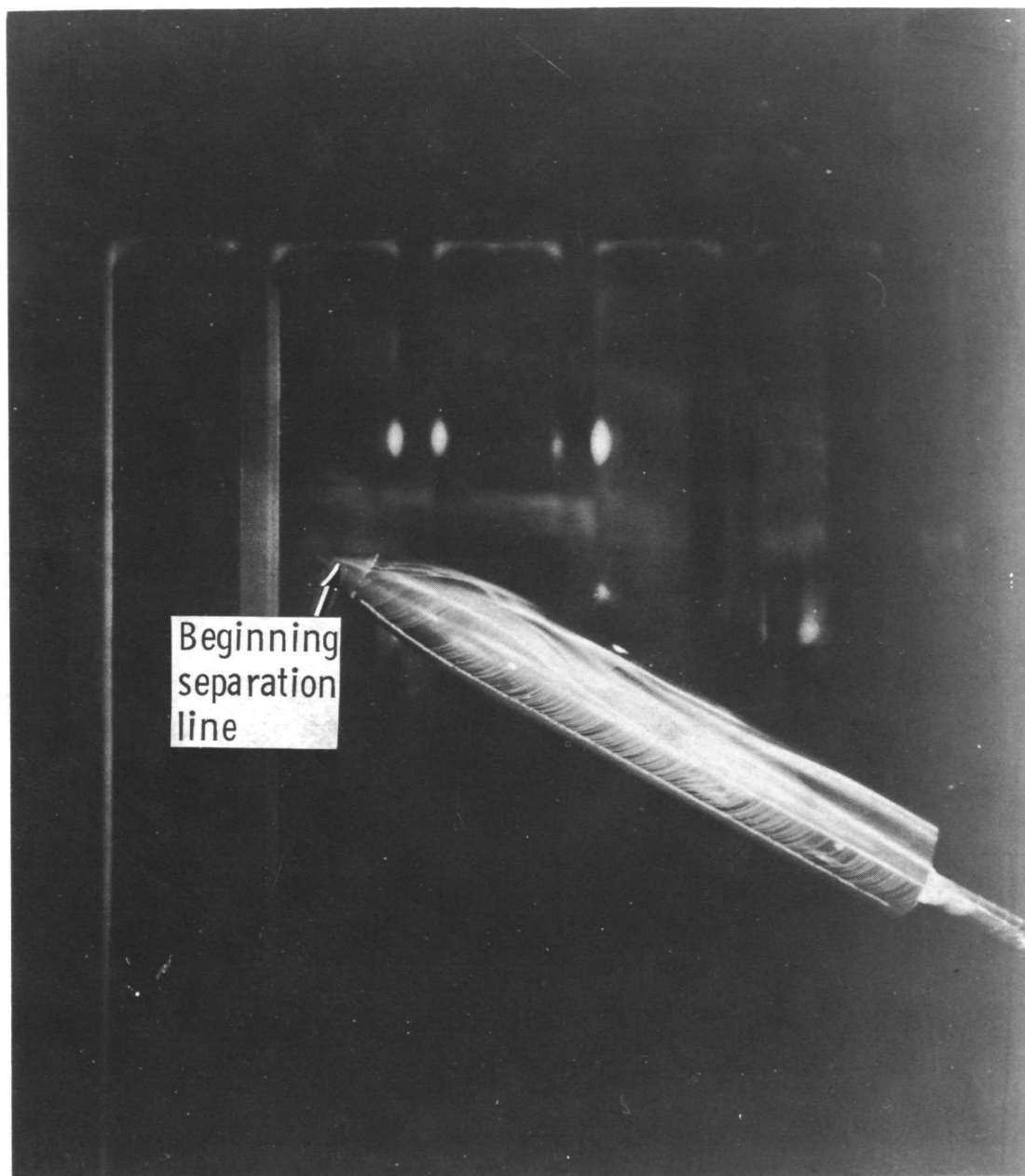
Figure 13.- Oil-flow photographs of model B at  $M = 2.16$ .



(b)  $\alpha = 20^\circ$ .

L-79-329

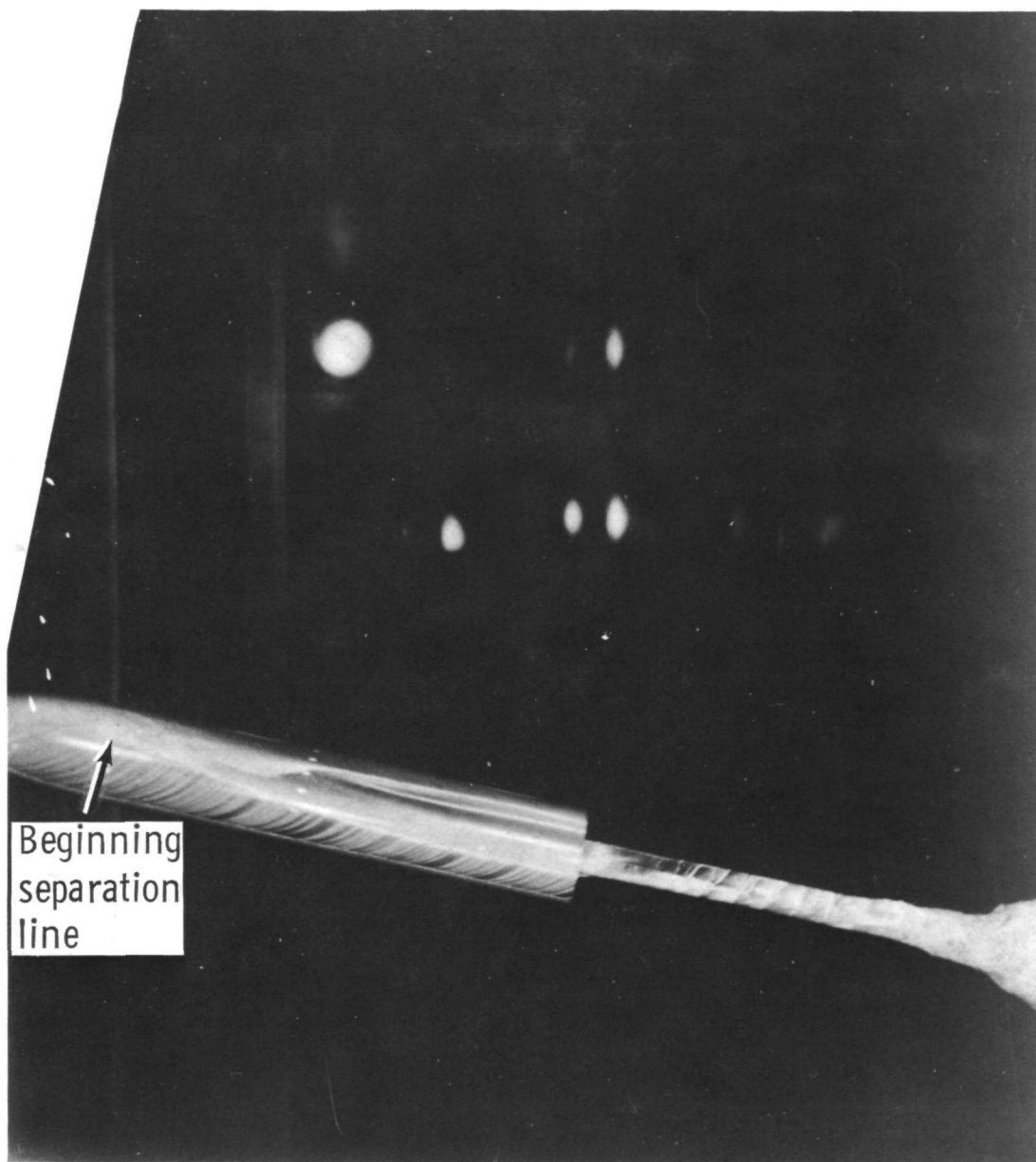
Figure 13.- Continued.



L-79-330

(c)  $\alpha = 30^\circ$ .

Figure 13.- Concluded.

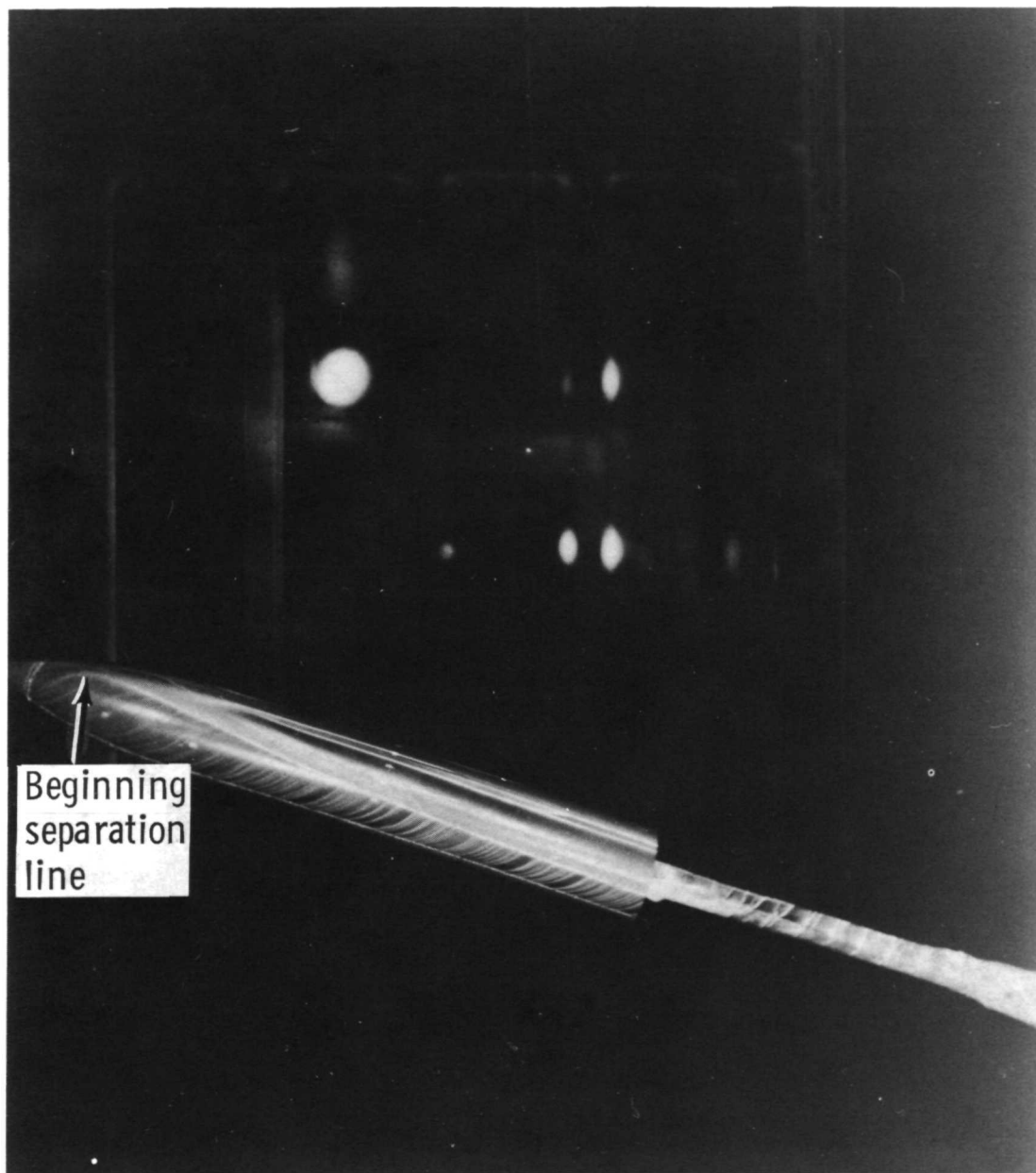


(a)  $\alpha = 15^\circ$ .

L-79-331

Figure 14.- Oil-flow photographs of model A at  $M = 2.16$ .

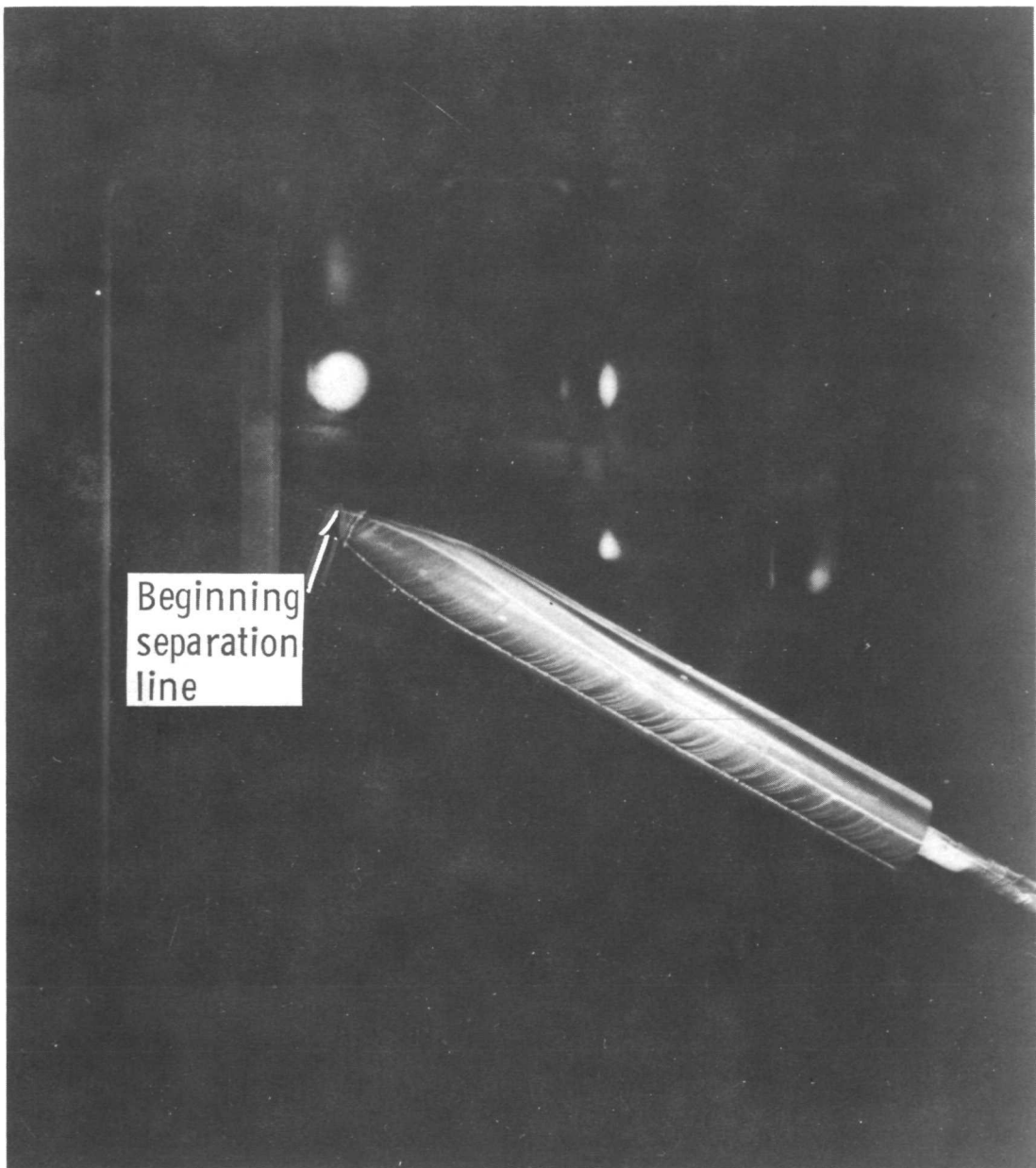




(b)  $\alpha = 20^\circ$ .

L-79-332

Figure 14. - Continued.



L-79-333

(c)  $\alpha = 30^\circ$ .

Figure 14.- Concluded.

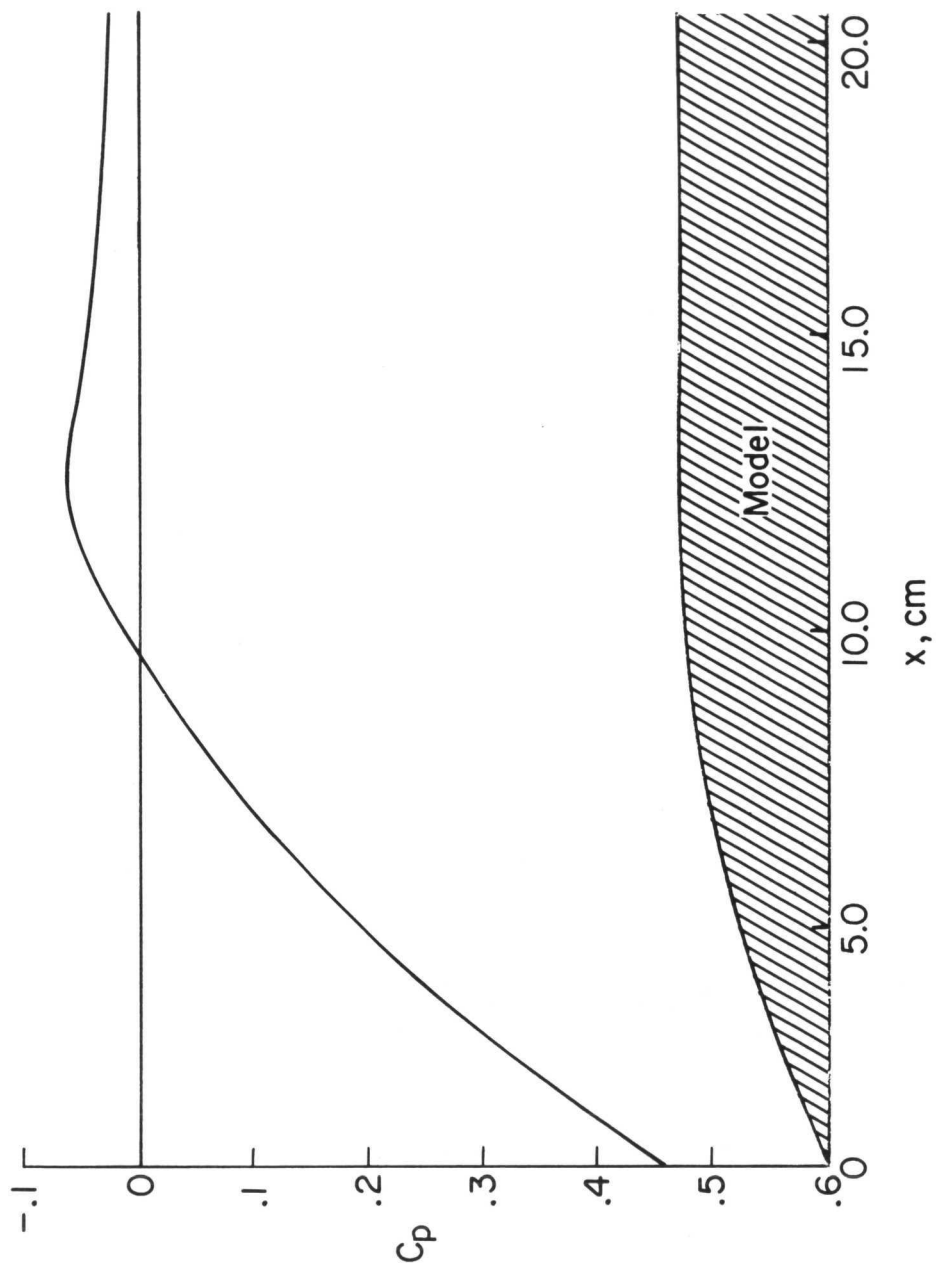
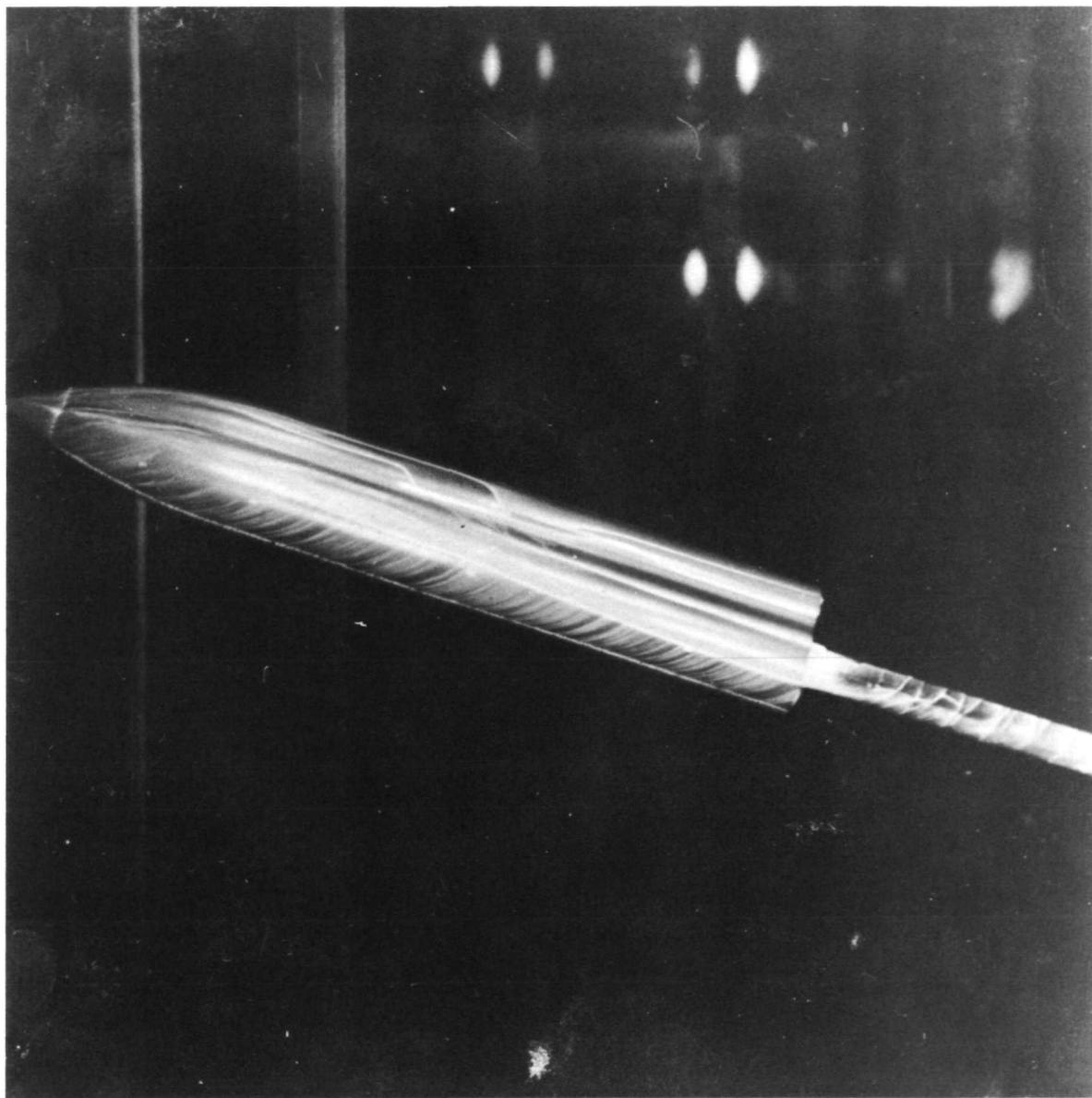


Figure 15.- Pressure distribution for model A at  $M = 2.16$  with  $\alpha = 0^\circ$ .



L-79-334

Figure 16.- Oil-flow photograph of model C at  $M = 2.16$  with  $\alpha = 20^\circ$ .

1. Report No. NASA TP-1579		2. Government Accession No.		3. Recipient's Catalog No.	
4. Title and Subtitle INVESTIGATION OF FLOW CHARACTERISTICS OVER MISSILE BODIES AT SUPERSONIC SPEEDS				5. Report Date December 1979	
				6. Performing Organization Code	
7. Author(s) Raymond L. Barger and Wallace C. Sawyer				8. Performing Organization Report No. L-13224	
9. Performing Organization Name and Address NASA Langley Research Center Hampton, VA 23665				10. Work Unit No. 505-43-23-02	
				11. Contract or Grant No.	
				13. Type of Report and Period Covered Technical Paper	
12. Sponsoring Agency Name and Address National Aeronautics and Space Administration Washington, DC 20546				14. Sponsoring Agency Code	
15. Supplementary Notes					
16. Abstract  Three missile body shapes were tested at Mach numbers of 1.50, 2.16, and 2.86 with angles of attack up to 30°. At moderate angles of attack, the flow was not characterized by a uniform pattern or by periodic vortex shedding. Flow visualization indicated cumulative effects due to shed vorticity. The pitching-moment variation was a sensitive indicator of incipient separation. Vortex effects were observed more readily with oil-flow visualization than with vapor-screen or schlieren methods. The cross-flow drag appeared to be primarily a function of cross-flow fineness ratio.					
17. Key Words (Suggested by Author(s)) Missile body shapes Nonaxisymmetric Separation visualization Flow visualization				18. Distribution Statement Unclassified - Unlimited  Subject Category 02	
19. Security Classif. (of this report) Unclassified	20. Security Classif. (of this page) Unclassified	21. No. of Pages 38	22. Price* \$4.50		

National Aeronautics and  
Space Administration

THIRD-CLASS BULK RATE

Postage and Fees Paid  
National Aeronautics and  
Space Administration  
NASA-451



Washington, D.C.  
20546

Official Business

Penalty for Private Use, \$300

**NASA**

POSTMASTER: If Undeliverable (Section 158  
Postal Manual) Do Not Return

---